Carbon nanotubes: properties and application

Valentin N. Popov[1]

Laboratoire de Physique du Solide, Facultés Universitaires Notre-Dame de la Paix, B-5000 Namur, Belgium

Abstract

Carbon nanotubes are unique tubular structures of nanometer diameter and large length/diameter ratio. The nanotubes may consist of one up to tens and hundreds of concentric shells of carbons with adjacent shells separation of ∼0.34 nm. The carbon network of the shells is closely related to the honeycomb arrangement of the carbon atoms in the graphite sheets. The amazing mechanical and electronic properties of the nanotubes stem in their quasi-one-dimensional (1D) structure and the graphite-like arrangement of the carbon atoms in the shells. Thus, the nanotubes have high Young's modulus and tensile strength, which makes them preferable for composite materials with improved mechanical properties. The nanotubes can be metallic or semiconducting depending on their structural parameters. This opens the ways for application of the nanotubes as central elements in electronic devices including field-effect transistors (FET), single-electron transistors and rectifying diodes. Possibilities for using of the nanotubes as high-capacity hydrogen storage media were also considered. This report is intended to summarize some of the major achievements in the field of the carbon nanotube research both experimental and theoretical in connection with the possible industrial applications of the nanotubes.
© 2003 Published by Elsevier B.V.

Keywords: Carbon nanotubes; Synthesis; Growth; Optical properties; Transport; Vibrational properties; Thermal properties; Nanodevices

1. Introduction

Elemental carbon in the sp^2 hybridization can form a variety of amazing structures. Apart from the well-known graphite, carbon can build closed and open cages with honeycomb atomic arrangement. First such structure to be discovered was the C$_{60}$ molecule by Kroto et al. [1]. Although various carbon cages were studied, it was only in 1991, when Iijima [2] observed for the first time tubular carbon structures. The nanotubes consisted of up to several tens of graphitic shells (so-called multi-walled carbon nanotubes (MWNTs)) with adjacent shell separation of ∼0.34 nm, diameters of ∼1 nm and large length/diameter ratio. Two years later, Iijima and Ichihashi [3] and Bethune et al. [4] synthesized single-walled carbon nanotubes (SWNTs) (Fig. 1). Nowadays, MWNTs and SWNTs are produced mainly by three techniques: arc-discharge, laser-ablation, and catalytic growth. The synthesized nanotube samples are characterized by means of Raman, electronic, and optical spectroscopies. Important information is derived by mechanical, electrical and thermal measurements. The experimental data is discussed in comparison with the results of theoretical models and computer simulations (see, e.g. [7–9]).

E-mail address: vpopov@phys.uni-sofia.bg (V.N. Popov).
[1] Permanent address: Faculty of Physics, University of Sofia, BG-1164 Sofia, Bulgaria.
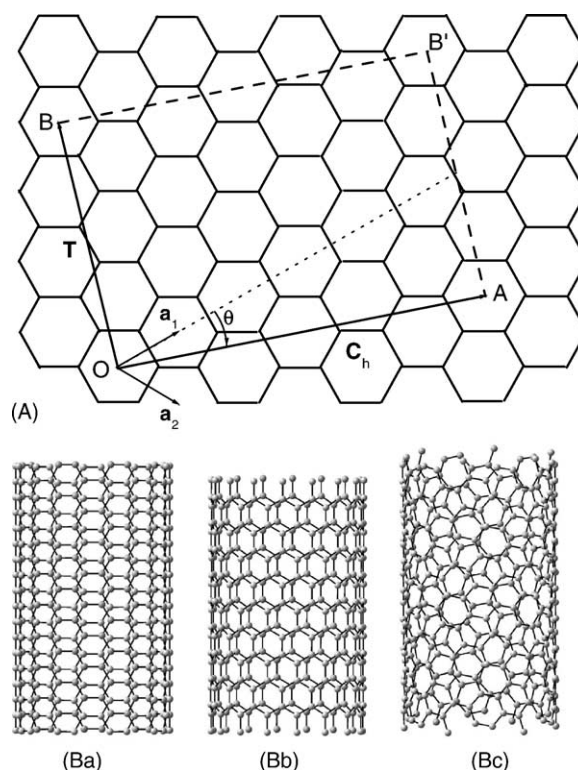
Fig. 1. Schematic representation of the construction of a nanotube by rolling-up an infinite strip of graphite sheet (so-called graphene). In (A) the chiral vector $C_h = na_1 + ma_2$ connects two lattice points O and A on the graphene sheet. An infinite strip is cut from the sheet through these two points, perpendicular to the chiral vector. The strip is then rolled-up into a seamless cylinder. $T = t_1a_1 + t_2a_2$ is the primitive translation vector of the tube [5]. The nanotube is uniquely specified by the pair of integer numbers n, m or by its radius $R = C_h/2\pi$ and chiral angle θ which is the angle between C_h and the nearest zigzag of C–C bonds. All different tubes have angles θ between zero and 30°. Special tube types are the achiral tubes (tubes with mirror symmetry): armchair tubes (n, n) ($\theta = 30°$) (B(a)) and zigzag tubes $(n, 0)$ ($\theta = 0°$) (B(b)). All other tubes are called chiral (B(c)). Details about relations between structural parameters of SWNTs can be found in [6].

Along with the improvement of the production and characterization techniques for nanotubes, progress is being made in their application. The estimated high Young's modulus and tensile strength of the nanotubes has lead to speculations for their possible use in composite materials with improved mechanical properties [10]. Nanotubes are suitable as electron field emitters because of their nanosize, structural perfection, high electrical conductivity, and chemical stability with an application in flat panel displays [11]. Multiwall nanotubes have been used to electro-catalyze an oxygen reduction reaction, which is important for fuel cells [12]. Electrochemically Li-intercalated SWNT materials showed large irreversible capacities and voltage hysteresis which is an advantage for using them as battery electrodes [13]. The extraordinary high and reversible hydrogen adsorption in SWNT materials has attracted much attention because of the possibility of using nanotubes as high-capacity hydrogen storage media [14]. It was proposed to use nanotubes as central elements of electronic devices including field-effect transistors, single-electron transistors and rectifying diodes [15] and for logic circuits [16].

This paper is intended to summarize the major achievements in the field of the nanotube research both experimental and theoretical in connection with the possible industrial applications of the nanotubes. The paper is organized as follows. Section 2 focuses on the synthesis of carbon

nanotubes. Section 3 considers possible growth mechanisms of nanotubes. Section 4 deals with the electronic band structure of the nanotubes and their optical properties. Section 5 reviews transport through ideal nanotubes and Section 6 considers transport through nanotube junctions. Section 7 presents the theory of the phonon dispersion in nanotubes and Raman spectroscopy. Section 8 surveys the mechanical properties of nanotubes. Finally, Section 9 deals with the thermal properties of nanotubes. The report ends with a summary.

2. Synthesis of CNTs

The MWNTs were first discovered in the soot of the arc-discharge method by Iijima [2]. This method has been used long before that in the production of carbon fibers and fullerenes. It took 2 years to Iijima and Ichihashi [3], and Bethune et al. [4] to synthesize SWNTs by use of metal catalysts in the arc-discharge method in 1993. A significant progress was achieved by laser-ablation synthesis of bundles of aligned SWNTs with small diameter distribution by Smalley and co-workers [17]. Catalytic growth of nanotubes by the chemical vapor decomposition (CVD) method was first used by Yacaman et al. [18]. The industrial application of the carbon nanotubes requires the development of techniques for large-scale production of defect-free nanotubes. In this section, the major progress in the in the nanotube production methods will be outlined, first, in historical plan, and, secondly, the three main production techniques will be considered separately.

2.1. Arc-discharge

In 1991, Iijima reported the preparation of a new type of finite carbon structures consisting of needle-like tubes [2]. The tubes were produced using an arc-discharge evaporation method similar to that used for the fullerene synthesis. The carbon needles, ranging from 4 to 30 nm in diameter and up to 1 μm in length, were grown on the negative end of the carbon electrode used for the direct current (dc) arc-discharge evaporation of carbon in an argon-filled vessel (100 Torr) (see Fig. 2). Transmission electron microscopy (TEM) revealed that each of the needles comprised coaxial tubes of graphitic sheets, ranging in number from 2 to about 50, later called multi-walled carbon nanotubes. On each of the tubes the carbon-atom hexagons were arranged in a helical fashion about
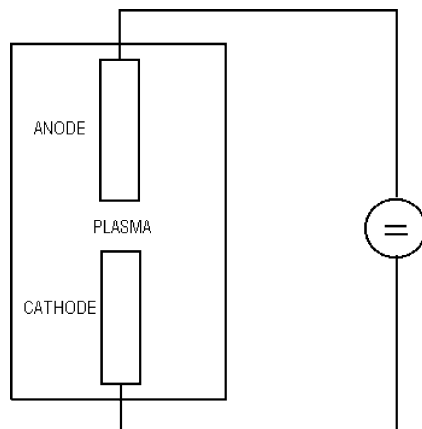

Fig. 2. Arc-discharge scheme. Two graphite electrodes are used to produce a dc electric arc-discharge in inert gas atmosphere.

the needle axis. The helical pitch varied from needle to needle and from tube to tube within a single needle. The tips of the needles were usually closed by curved, polygonal, or cone-shaped caps. A growth model was proposed in which the individual tubes have spiral growth steps at the tube ends.

The TEM study of the growth morphology of the carbon microtubules synthesized by arc-discharge [19] revealed that there were many variations in shape, especially near the tube tips. A topological model was constructed in which pentagons and heptagons played a key role in the tube-tip shapes. Iijima et al. [20] proposed a model for an open-ended growth, in which the carbon atoms are captured by the dangling bonds, and a layer-by-layer growth, in which the nanotubes thickens. The nucleation of positive (pentagons) and negative (heptagons) disclinations on open-tube ends results in changes of growth directions, producing different morphologies.

Large-scale synthesis of MWNTs by a variant of the standard arc-discharge technique was reported by Ebbesen and Ajayan [21]. A potential of ∼18 V dc was applied between two thin graphite rods in helium atmosphere. At helium pressure of ∼500 Torr, the yield of nanotubes was maximal of ∼75% relative to the starting graphitic material. The TEM analysis revealed that the samples consisted of nanotubes of two or more concentric carbon shells. The nanotubes had diameters between 2 and 20 nm, and lengths of several micrometers. The tube tips were usually capped with pentagons.

In 1993, Iijima and Ichihashi [3] and Bethune et al. [4] almost simultaneously reported the arc-discharge and catalyst-assisted synthesis of SWNTs. Iijima used arc-discharge chamber filled with a gas mixture of 10 Torr methane and 40 Torr argon. Two vertical thin electrodes were installed in the center of the chamber. The lower electrode, the cathode, had a shallow dip to hold a small piece of iron during the evaporation. The arc-discharge was generated by running a dc current of 200 A at 20 V between the electrodes. The use of the three components—argon, iron and methane, was critical for the synthesis of SWNTs. The TEM analysis of the obtained specimens revealed the presence of SWNT threads, which were curved and tangled together to form bundles. The nanotubes had diameters of ∼1 nm with a broad diameter distribution between 0.7 and 1.65 nm.

In the arc-discharge synthesis of nanotubes, Bethune et al. [4] used as anodes thin electrodes with bored holes which were filled with a mixture of pure powdered metals (Fe, Ni or Co) and graphite. The electrodes were vaporized with a current of 95–105 A in 100–500 Torr of He. The TEM analysis of the obtained specimens showed that only cobalt-catalyzed nanotubes had single-atomic-layer walls with uniform diameters of 1.2 ± 0.1 nm.

Large quantities of SWNTs were generated by the arc-technique by Journet et al. [22]. The arc was generated between two graphite electrodes in a reactor under helium atmosphere (660 mbar). The anode had a hole drilled in its end, filled with a mixture of metallic catalyst (Ni-Co, Co-Y, or Ni-Y) and graphite powder. The arc was created by a current of 100 A at a constant voltage drop of 30 V. By scanning electron microscopy (SEM), the deposited material was seen to consist of large amounts (∼80%) of entangled carbon ropes. The high-resolution TEM images showed that the ropes had diameters from 5 to 20 nm. The tube diameters were around 1.4 nm with average separations of ∼1.7 nm. The X-ray diffraction (XRD) patterns showed periodic arrangement of the tubes in the ropes. The similarity of the X-ray diffraction data by Journet et al. [22] and Thess et al. [17] (laser-ablation, see below) was clearly observed: yields in the range 70–90%, tube diameter around 1.4 nm, crystalline bundles of few tens of nanotubes. This lead to the conclusion of a unique growth mechanism in both cases which does not depend on the details of the experimental conditions, but which depends much more on the kinetics of carbon condensation in a non-equilibrium situation. Among the two methods, the arc-discharge one has the advantage of being much cheaper than the laser-ablation method.
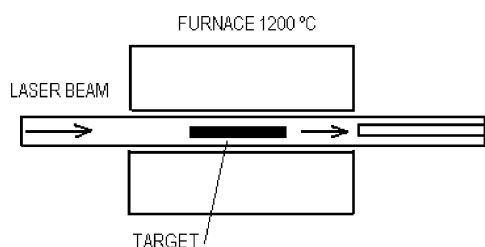
Fig. 3. Laser-ablation scheme. Laser beam vaporizes target of a mixture of graphite and metal catalyst (Co, Ni) in a horizontal tube in a flow of inert gas at controlled pressure and in a tube furnace at ∼1200 °C. The nanotubes are deposited on a water-cooled collector outside the furnace.

2.2. Laser-ablation

In 1996, Smalley and co-workers produced high yields (>70%) of SWNTs by laser-ablation (vaporization) of graphite rods with small amounts of Ni and Co at 1200 °C [17] (see Fig. 3). The X-ray diffraction and TEM showed that the synthesized nanotubes were remarkably uniform in diameters and that they formed ropes (or bundles) 5–20 nm in diameter and tens to hundreds of micrometers long. The ropes formed a two-dimensional (2D) triangular lattice with lattice constant $a = 1.7$ nm through van der Waals bonding. The ropes were metallic and it was argued that a particular tube (10, 10), might be the dominant component. The growth of the nanotubes was explained by a ''scooter'' mechanism (Fig. 4). In this mechanism a single Ni or Co atom chemisorbs onto the open edge of a nanotube. The metal atom must have a sufficiently high electronegativity as to prevent formation of fullerenes and it must be highly effective in catalyzing the nanotube growth. The metal atom circulates (''scoots'') around the open-end of the tube and absorbs small carbon molecules and converts them into graphite-like sheet. The tube grows until too many catalyst atoms aggregate on the end of the nanotube. The large particles either detach or become over-coated with sufficient carbon to poison the catalysis. This allows the tube to terminate with a fullerene-like tip or with a catalyst particle. It was argued that the scooter mechanism favors the growth of armchair type nanotubes with of most probable type (10, 10) which corresponds to the experimental observations.
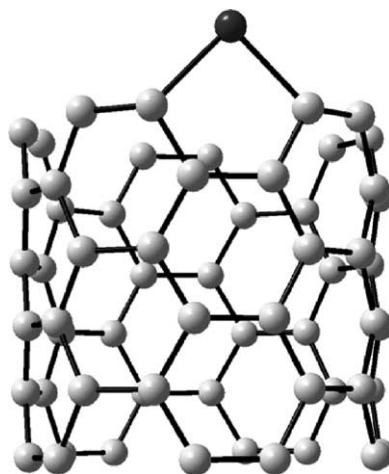

Fig. 4. Illustration of the ''scooter'' mechanism for growth in the case of a (10, 10) SWNT assisted by a Ni atom chemisorbed onto the open edge of the nanotube (after [17]).

Both arc-discharge and laser-ablation techniques have the advantage of high (>70%) yields of SWNTs and the drawback that (1) they rely on evaporation of carbon atoms from solid targets at temperatures >3000 °C, and (2) the nanotubes are tangled which makes difficult the purification and application of the samples.

The laser-ablation prepared samples usually contain >70% nearly endless, highly tangled ropes of SWNTs along with nanoscale impurities. The potential use of the nanotubes in nanoelectronic devices requires nanotubes with length in the range of 10–300 nm. A procedure of purification of the as-grown sample before cutting the nanotube was proposed by Liu et al. [23] The purification method consists in refluxing in 2.6 M nitric acid and resuspending the nanotubes in pH 10 water with surfactant followed by filtration with a cross-flow filtration system. Passing the resultant purified SWNT suspension through a polytetrafluoroethylene filter produced a freestanding mat of tangled SWNT ropes—a ''bucky paper''. Several cutting techniques were proposed, the most efficient of which was prolonged sonification of the nitric acid-purified SWNT rope material in a mixture of concentrated sulfuric and nitric acids at 40 °C.

2.3. Catalytic growth

Carbon filaments and fibers have been produced by thermal decomposition (or chemical vapor decomposition) of hydrocarbons in the presence of a catalyst since the 1960s (see, e.g. [24,25]). A similar approach was used for the first time by Yacaman et al. [18] in 1993 and in 1994 Ivanov and co-workers [26,27] to grow MWNTs. The CVD technique has been subsequently improved and optimized. Generally, the CVD process includes catalyst-assisted decomposition of hydrocarbons, usually ethylene or acetylene, in a tube reactor at 550–750 °C and growth of carbon nanotubes over the catalyst upon cooling the system (see Fig. 5). Best results are obtained with Fe, Ni or Co nanoparticles as catalyst. The same catalysts are found optimal in the arc-discharge and laser-ablation techniques, which is in favor of a common nanotube growth mechanism. It was argued that the nanotubes grow out of the catalyst nanoparticle embedded in the pores by tip growth or base growth depending on the contact force between the catalyst particles and the substrate [24,27].

Large-scale synthesis of aligned carbon nanotubes was achieved by the CVD technique and iron as catalyst by Li et al. [28]. A substrate containing iron nanoparticles embedded in mesoporous silica was placed in the reaction chamber. A mixture of 9% acetylene in nitrogen was introduced in the chamber at a flow rate of 110 cm^3/min. Carbon nanotubes were formed on the substrate containing the iron nanoparticles by deposition of carbon atoms obtained by decomposition of acetylene at 700 °C. The samples were examined by SEM and energy-dispersive X-ray diffraction (EDX). The SEM image of the obtained thin films showed that nanotubes grew continuously from the bottom to the top of the film in lengths between 50 and 100 μm. The nanotubes were multi-walled with outer diameters of ∼30 nm and consisting of ∼40 shells, and formed arrays with nanotube spacing of
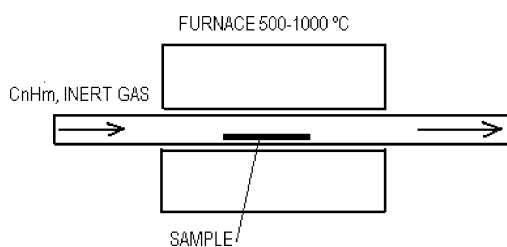

Fig. 5. Catalytic growth scheme. Hydrocarbon gas is decomposed in a quartz tube in a furnace at 550–750 °C over a transition metal catalyst (a CVD reactor).

~100 nm, consistent with the spacing between the pores on the substrate. It could not be determined which one of the two so far proposed growth mechanisms—tip growth or base growth, was realized.

Porous silicon wafer was used in a CVD method to grow a regular array of MWNTs [29]. The porous silicon was obtained by electrochemical etching of heavily doped n^+ type Si wafers. The substrates were patterned with Fe films by electron beam evaporation through shallow masks with squared openings with side length 10–250 μm at pitch distances of 50–200 μm. The TEM images showed that the nanotubes had diameters of 16 nm formed on top of the patterned iron squares on the substrate. The CVD process was performed in a tube reactor at 700 °C in flowing argon, the carbon feedstock was ethylene.

High-quality SWNTs could be grown on silicon wafers patterned with micrometerscale islands of catalytic material by the CVD technique by Kong et al. [30]. Methane was used as carbon feedstock, high reaction temperatures in the range of 850–1000 °C were necessary to form small-diameter SWNTs. The optimal choice of a catalyst was a Fe/Mo species supported on a sol–gel derived alumina-silica multicomponent material. The TEM images revealed an abundance of individual and bundled SWNT. The SEM images showed that the SWNTs were of high quality with diameter distribution between 0.7 and 5 nm with a peak at 1.7 nm. The high yield of nanotubes (~47%) in this CVD method was found to be due to the increased metal–support interactions which favored base-mode nanotube growth. On the other hand, catalysts with weaker metal–support interactions lead to aggregation of metal nanoparticles and reduced nanotube yield and purity.

3. Growth mechanisms

It has been established experimentally that transition metal catalysts are necessary for the growth of SWNTs but are not required for MWNTs. This fact suggests different growth mechanisms in both cases. The role of the growth conditions on the structural characteristics of the obtained samples were studied both on experimental and theoretical levels. In this Section, the growth mechanisms for individual and bundled, single-walled and multi-walled nanotubes, studied within semi-empirical and ab initio approached will be reviewed.

3.1. Multi-walled nanotubes

Experimentally it is observed that the MWNTs grow both lengthening and thickening, and at some stage the nanotubes tend to close. Secondly, during the growth, the nanotubes remain open [20] although the large number of dangling bonds at the ends favor closing of the tubes. It was suggested that open-ended growth could be explained by a so-called lip–lip interaction [31] (Fig. 6). Tight-binding calculations on MWNTs showed that the growing edge is stabilized by bridging carbon atoms thus prolonging the life of the open structure. First-principles molecular-dynamics simulations on SWNTs and double-walled nanotubes (DWNTs) were performed in order to understand the growth process [32,33]. At experimental temperatures the open-end of SWNTs closed spontaneously into a graphitic dome in accordance with the experimental fact that SWNTs do not grow in the absence of transition metal catalysts. The tip closure resulted in a substantial reduction in the localized density of electronic states on the tips close to the Fermi energy. This result suggested that the reactivity of closed nanotube tips should be considerably lower than that of open-end nanotubes. This result ruled out the possibility of SWNT growth by sustained incorporation of carbon atoms into the closed tip. On the other hand, chemical bonding between the edges of adjacent walls trapped at the end of a DWNT in a metastable energy minimum. This lip–lip interaction inhibited dome
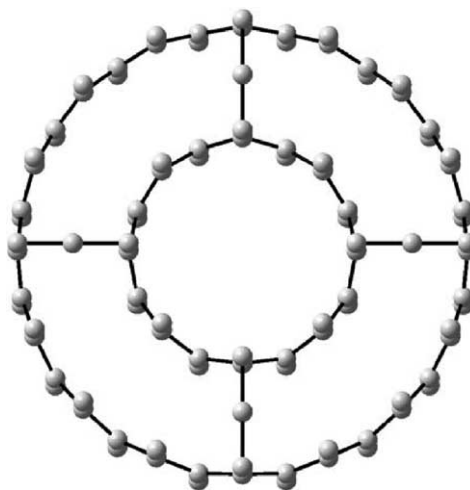
Fig. 6. Lip–lip growth mechanism scheme representing a top view of a double-walled nanotube with an open zigzag edge. The adatoms occupying sites between doubly coordinated edge atoms of adjacent walls stabilize open-tube growth (after [31]).

closure. The bridging bonds were found to continuously break and re-form which facilitated the rapid absorption of carbon atoms by the nanotube edges.

In the study of the morphology and the structural stability of the growing edge of MWNTs by use of ab initio and parameterized calculations it was found that strong covalent bonds connecting the exposed edges of adjacent walls stabilize the nanotubes against dome closure [34]. In another computer simulation, a realistic many-body potential was used to investigate the role of lip–lip interactions on the growth of DWNTs [35]. Surprisingly, the lip–lip interaction did not stabilize open-end growth but rather facilitated tube closure by mediating the transfer of atoms between inner and outer shells. Additionally, the simulation of the growth on a wide DWNT lead to considerable deviations from the ideal structure. It was suggested that there could be other mechanisms than the lip–lip interaction contributing to the open-end growth of MWNTs.

3.2. Single-walled nanotubes

The growth of SWNTs with a narrow diameter distribution by the arc-discharge [22] and the laser-ablation techniques [17] requires and critically depends on the composition of the catalyst. By classical molecular-dynamics simulations using realistic many-body carbon–carbon potentials [36] it was shown that wide nanotubes, which are initially open, continue to grow maintaining the hexagonal structure. However, nanotubes narrower than a critical diameter of about 3 nm, grew curved with pentagonal structures, which lead to tube closure. First-principles molecular-dynamics simulations [32] show that the open-end of small diameter SWNTs close spontaneously at experimental temperatures of 2000–3000 K into a graphitic dome with no residual dangling bonds (Fig. 7). The reactivity of the closed nanotube tips was found to be considerably reduced compared to that of open-end nanotubes. It was concluded that it is unlikely that SWNTs could grow by sustained incorporation of carbon atoms on the closed hemifullerene-like tip.

The synthesis of nanotubes with small diameters ~1.4 nm requires catalyst and it is necessary to clarify the role of the catalyst in the nanotube growth. There are plausible suggestions for the explanation of the catalytic growth but for the time being it has not been
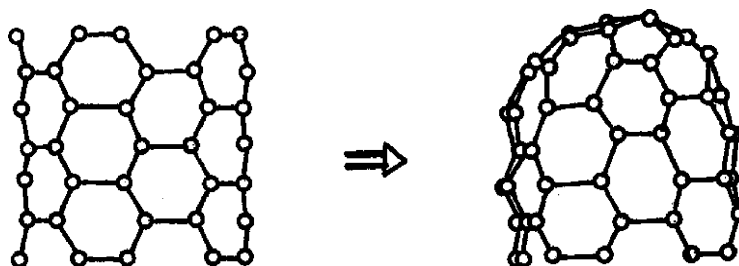
Fig. 7. Spontaneous closure of a (5, 5) armchair tube. The dangling bonds at the bottom are passivated by hydrogen atoms. Forming pentagon structures at the top of the nanotube leads to dome closure (after [32]).

clearly understood. The most probable mechanism of catalyst-assisted tip-growth assumes that the metal atoms sit on the open edge of precursor fullerene clusters [17]. The metal atoms ''scoot'' around the open edge of the cluster preventing the formation of carbon pentagons and the dome closure (Fig. 6). Static ab initio calculations have shown that Co or Ni atom is indeed strongly bound to the open edge of the nanotube but is still very mobile on it [37]. The metal atom locally inhibits the formation of pentagons that would initiate dome closure. Additionally, the metal catalyst assists incoming carbon atoms in the formation of hexagons and thus in the lengthening of the tube. With time the metal atoms at the tube edge will tend to aggregate. It is found that the adsorptive energy per metal atom decreases with the increase of the size of the adsorbed metal cluster. These clusters will become gradually less reactive and less mobile. Eventually, when the size of the metal cluster reaches some critical value, the adsorption energy of the cluster will decrease to such a level that it will peel off the edge. In the absence of the catalyst at the tube edge, defects can no longer be annealed effectively, thus initiating tube closure. This mechanism is consistent with the experimental observation that no metal particle could be found on the grown tubes [17].

Another possible mechanism is the catalyst-assisted base (or root) growth of SWNTs. In laser-ablation of graphite powders in the presence of Ni and/or Co catalyst, high yield bundled SWNTs with wide range of chirality angles were produced [38]. The TEM images showed that the bases of the nanotubes were terminated into nanoparticles consisting of carbon and metal atoms, which were formed during the laser-ablation process. It was suggested that the nanoparticles, often with dangling bonds, could catalyze the growth of SWNTs by adding carbon atoms to the tubes. In order to clarify the base growth mechanism, molecular-dynamics and total-energy calculations using a realistic three-body potential for carbon were carried out [39]. It was found that nanometer-sized protrusions on the nanoparticle surface lead to nucleation of very narrow tubes. Wide bumps lead to a strained graphite sheet and no nanotube growth. In the simulations, the migration of a precipitated carbon atom on the graphite layer covering a nanoparticle was studied. The precipitated carbon atom was found to form a ''handle'' between a pair of nearest-neighbor carbon atoms on the layer (Fig. 8). The handle migrates to the energetically most favorable sites—at the root of the tube where there are mostly heptagons. The pair of handles on opposite bonds of a heptagon annihilate leading to the creation of additional hexagons and thus to a defect-free root growth mechanism (Fig. 9).

The two proposed mechanisms for catalyst-assisted growth of SWNTs only qualitatively describe the synthesis process. Yet a lot of theoretical and experimental investigations are needed in order to predict the growth mechanism in particular experimental conditions and to produce SWNTs with desirable properties.
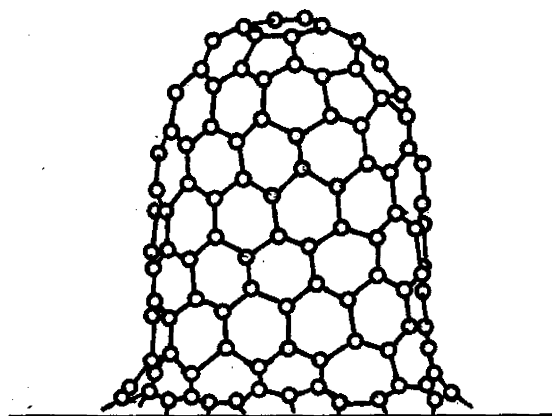
Fig. 8. Base growth mechanism scheme. The precipitated carbon atoms form ''handles'' which migrate to the root of the nanotube. These atoms are then incorporated into the hexagonal carbon network at the root of the tube (after [39]).
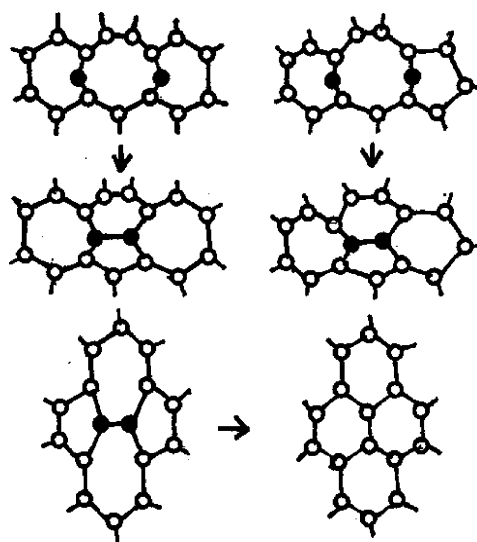

Fig. 9. Mechanism of hexagon addition at the nanotube-base by bond formation between a pair of handles atoms at the opposite sides of a heptagon (after [39]).

4. Optical properties

The early theoretical studies of the electronic properties of SWNTs predicted that SWNTs could be either metallic or semiconducting depending on their structural parameters [40–42]. In the π-tight-binding model within the zone-folding scheme, one third of the nanotubes are metallic and two thirds are semiconducting depending on their indices (n, m). The tight-binding calculations based on the use of σ and π bands, due to the curvature-induced mixing of these bands, predict that some metallic nanotubes to be very-small-gap semiconducting nanotubes [41,42]. In MWNTs and in bundles of SWNTs the lower symmetry of these structures with respect to the symmetry of the separate SWNTs leads to the appearance or disappearance of the band gap [43,44].

4.1. Electronic band structure of SWNTs

The band structure of the ''rolled-up'' SWNTs can be studied in a good approximation within the tight-binding model in the zone-folding scheme [42]. The band structure of a single graphene sheet is considered as a starting point. The unit cell of the sheet contains two carbon atoms, each carbon atom having four valence electrons. Therefore, a tight-binding model yields eight bands: four valence bands and four conduction bands. One s orbital and two in-plane p orbitals of each carbon atom are sp^2-hybridized. Due to the different symmetry of the sp^2-hybridized orbitals and p_z orbitals, the matrix elements of the Hamiltonian and the overlap matrix elements between such orbitals vanish. The sp^2-hybridized orbitals form the so-called σ valence bands and σ^* conduction bands. The p_z orbitals of the carbon atoms, oriented perpendicularly to the sheet (z-direction), form the π valence band and the π^* conduction band. Therefore, the problem for the band structure of a graphite sheet conveniently splits into a problem for the σ and σ^* bands, and a problem for the π and π^* bands. The latter problem is of major importance for the resonant Raman scattering and we will focus on it. The resulting band structure of graphene (Fig. 10) is characterized with π and π^* bands degenerate at the $\boldsymbol{K}$ points in the hexagonal Brillouin zone of the sheet. This degenerate energy level corresponds to the Fermi energy, which shows that the graphene sheet is a zero-gap metal. On rolling-up a graphene strip into a cylindrical nanotube, the band structure of the nanotube can be derived from that of the graphene sheet by the zone-folding method.

The one-dimensional (1D) band structure of a (n, m) nanotube is given by the zone-folding relation by use of the two-dimensional band structure of graphene [8]

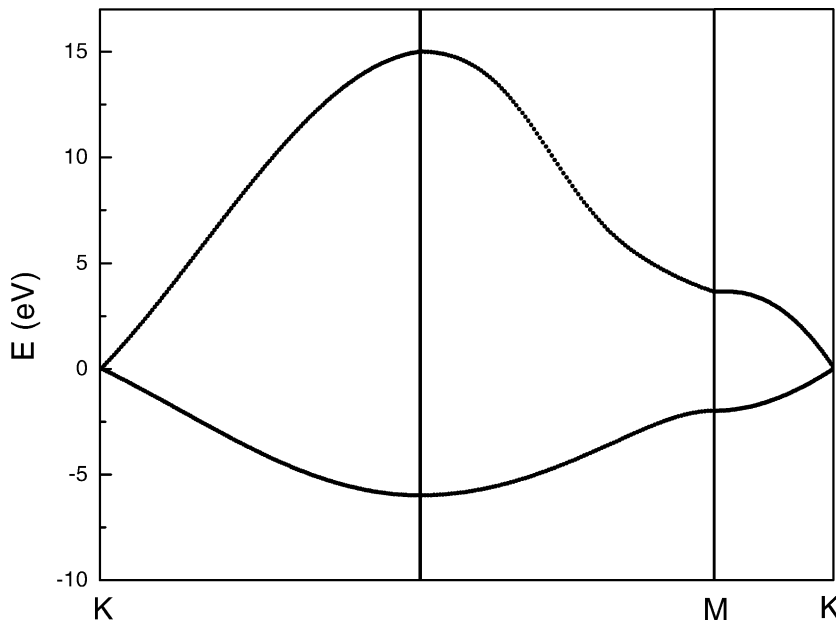$$E_{k\mu} = E_{2D}\left(k\frac{\boldsymbol{K}_2}{|\boldsymbol{K}_2|} + \mu\boldsymbol{K}_1\right).$$

Fig. 10. The electronic band structure of a graphite sheet calculated within a π-band tight-binding model. The valence π and conduction π^* bands show degeneracy at the $\boldsymbol{K}$ points in the Brillouin zone at the Fermi level.

Here k is the 1D wavevector ($-\pi/T < k < \pi/T$, T the translation period of the nanotube) and μ is a discrete quantum number ($\mu = 1, 2, \ldots, N$ where N is the number of carbon pairs in the unit cell of the nanotube). The vectors $\boldsymbol{K}_1$ and $\boldsymbol{K}_2$ are expressed through the reciprocal lattice vectors $\boldsymbol{b}_1$ and $\boldsymbol{b}_2$ of the graphene sheet as

$$\boldsymbol{K}_1 = \frac{-t_2\boldsymbol{b}_1 + t_1\boldsymbol{b}_2}{N} \quad \text{and} \quad \boldsymbol{K}_2 = \frac{m\boldsymbol{b}_1 - n\boldsymbol{b}_2}{N}.$$

The 1D band structure of a given SWNT consists of the 2D band structure of the graphene sheet along N lines along $\boldsymbol{K}_2$ in the 2D Brillouin zone of the sheet. If for a given nanotube one of these lines passes through a $\boldsymbol{K}$ point of this zone, the band structure of the nanotube will be characterized by a zero energy gap. If for a given nanotube none of these lines passes through a $\boldsymbol{K}$ point, the tube will have a finite energy gap. In the former case the tube is metallic and in the latter case it is semiconducting. In the zone-folding approach, a tube is metallic is n–m is a multiple of 3 and semiconducting if n–m is not a multiple of 3 [40–42] (Fig. 11).

The π-tight-binding model within the zone-folding scheme provides an approximate picture of the band structure of the SWNTs near the Fermi level. It totally ignores the effects of deviation from pure sp^2 hybridization due to tube curvature. This deviation leads to mixing of σ and π bands, which is significant for small diameter tubes. σ- and π-non-orthogonal-tight-binding calculations for the optimized nanotube structure show that only tubes (n, n) are metallic (zero-gap semiconductors), tubes (n, m) with n–m, which is a multiple of 3, are tiny-gap semiconductors, and all other tubes are large-gap semiconductors [41]. Ab initio pseudopotential DFT LDA calculations [45] reveal that strong rehybridization effects can occur in small radius nanotubes, which significantly alters their electronic structure. In the case of zigzag (n, 0) nanotubes ($n = 6, \ldots, 9$), a singly-degenerate band was calculated lower than with the tight-binding model of [41]. For a (6, 0) nanotube, this band crosses the highest valence band, predicting this tube to be metallic. For the nanotubes (7, 0) and (7, 0), only narrowing of the band gap was observed but for (9, 0) the band gap increased. For tubes
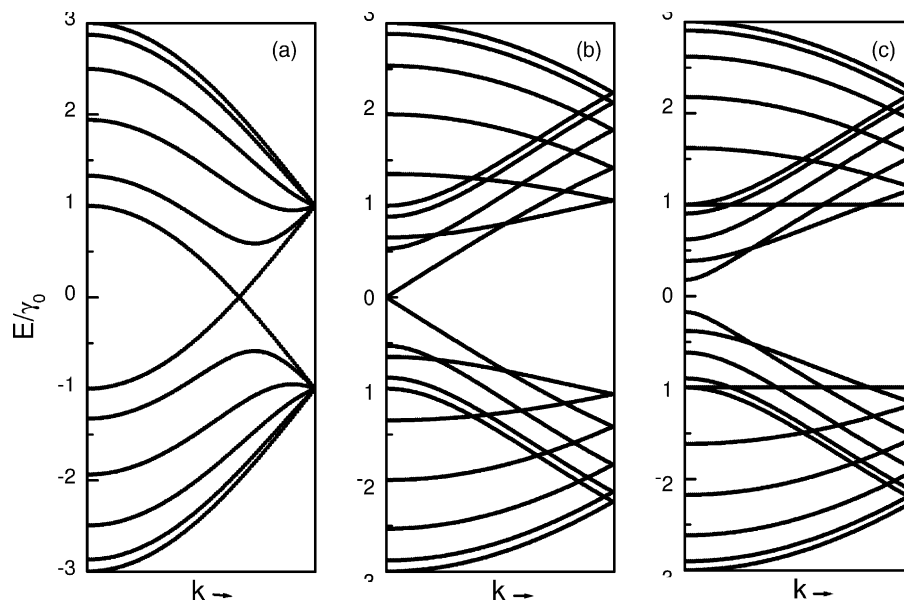

Fig. 11. Electronic band structure of nanotubes (a) (5, 5), (b) (9, 0) and (c) (10, 0) derived by zone-folding of the band structure of the graphene sheet; a is the nearest-neighbor C–C separation and $\gamma_0 = 2.9$ eV.

with diameters larger than 1 nm, the rehybridization effects were unimportant. The structural optimization of the nanotubes had little effect on the band structure. Tubes with diameters larger than 0.4 nm were found to be stable.

4.2. Electronic density of states of SWNTs

The metallic tubes have finite density of states (DOS) at the Fermi surface, which is inversely proportional to the tube diameter D [8]. The flat parts of the tube band energies give rise to two types van Hove singularities: $(E - E_0)^{-1/2}$ at the zone bottom and $(E_0 - E)^{-1/2}$ at the zone top. The light absorption coefficient and the resonant Raman scattering intensity require the calculation of the matrix elements of the momentum between states in the valence and the conduction band. The resultant intensity is non-zero for $\delta\mu = 0$ for light polarization parallel to the nanotube axis, and for $\delta\mu = \pm 1$ for light polarization perpendicular to the nanotube axis [46]. The optical transitions in the case of perpendicular geometry are largely suppressed by the depolarization effect. Therefore, the energy differences between the symmetrical pairs of van Hove spikes (bands with the same μ) have to be considered in the determining the resonant energy in the resonant Raman spectra corresponding to a particular nanotube diameter (Fig. 12). For tubes with large diameters D, the energy differences $E_{11}^M(D)$ and $E_{11}^S(D)$ for metallic (M) and semiconducting (S) nanotubes between the top of the highest-energy valence band and the bottom of the lowest-energy conduction band correspond to close $\boldsymbol{k}$ vectors in the Brillouin zone of the graphene sheet situated in the vicinity of the $\boldsymbol{K}$ point. These differences can be obtained from the π-tight-binding formula in the small $\boldsymbol{k}$-vector approximation, retaining the linear in $\boldsymbol{k}$ terms, as [47]

$$E_{11}^M(D) = \frac{6a_{C-C}\gamma_0}{D} \quad \text{and} \quad E_{11}^S(D) = \frac{2a_{C-C}\gamma_0}{D},$$

where a_{C-C} is the nearest-neighbor C–C separation and γ_0 is the hopping matrix element.

In this approximation, the separation between the "11" spikes in the DOS depends only on the tube diameter (first and third curves from below in Fig. 12). For tubes with small diameters, the top
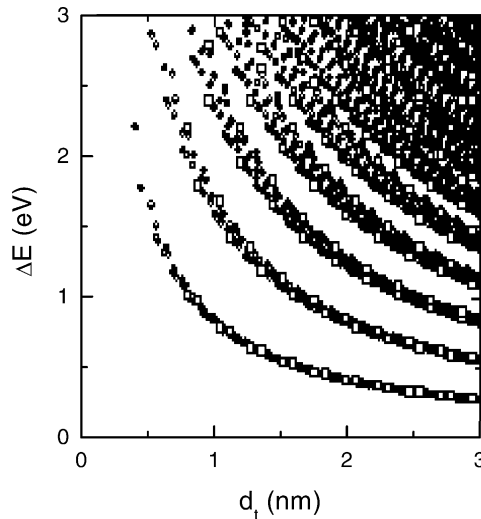

Fig. 12. The energy difference ΔE between the symmetrical spikes in the 1D DOS of SWNTs as a function of tube diameter d_t for all tube types with diameters between 0.7 and 3.0 nm (after [48]).

and the bottom of the mentioned conduction and valence bands, respectively, correspond to points in the Brillouin zone of the graphene sheet, for which the band energy is no longer isotropic. The equi-energy lines become triangles, a distortion known in structures with three-fold symmetry axis as the trigonal warping effect. The energy differences $E_{11}^M(D)$ and $E_{11}^S(D)$ will then depend on the direction of the tube axis on the graphite sheet and will therefore depend on the tube chirality as well. In the case of metallic nanotubes, the warping effect gives rise to DOS splitting of the first valence and conduction band spikes which is largest for zigzag nanotubes and zero for armchair nanotubes while having intermediate values for chiral nanotubes. The DOS splitting yields widening of the differences $E_{11}^M(D)$ and $E_{11}^S(D)$ for small diameter tubes. The trigonal warping effect is important for metallic zigzag nanotubes with $D < 2$ nm. Semiconducting nanotubes do not show trigonal warping effect.

4.3. Electronic band structure of SWNT bundles and MWNTs

The electronic properties of bundles of SWNTs can be derived from those of the constituent SWNTs supposing that the intertube interactions are weak enough not to change the band structure of the bundles significantly. First-principles calculations show that a broken symmetry of the (10, 10) tube caused by interactions between tubes in a bundle induces a pseudogap of about 0.2 eV [49] and 0.1 eV [44] at the Fermi level (Fig. 13). The mirror symmetry of isolated tubes (10, 10) leads to a doubly-degenerate state at the crossing of the π and π^* bands at the Fermi level. In a bundle, this symmetry is broken because of intertube interactions. The broken symmetry causes repulsion of the bands and opening a gap in the Brillouin zone. This pseudogap strongly modifies many of the fundamental electronic properties, e.g., semimetal-like temperature dependence of the electrical conductivity and a finite gap in the infrared absorption spectrum is predicted. It is concluded that the existence of both electron and hole carriers will result in a qualitatively different thermopower and Hall-effect behaviors from those expected for a normal metal.

Kwon et al. calculated the potential energy surface, the low-frequency vibrational modes, and the electronic structure of a (5, 5) at (10, 10) double-walled carbon nanotube within an accurate tight-binding model [49]. It was found that an energy gap or four pseudogaps open near the Fermi level during the soft librational motion with frequency ~ 30 cm^{-1}.
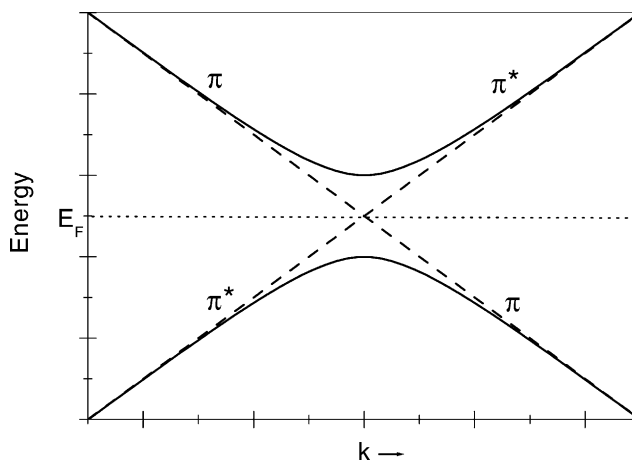

Fig. 13. Band crossing and band repulsion: (a) schematic band structure of an isolated (n, n) SWNT near the Fermi level (dashed lines) and (b) repulsion of bands due to the breaking of the mirror symmetry (solid lines).
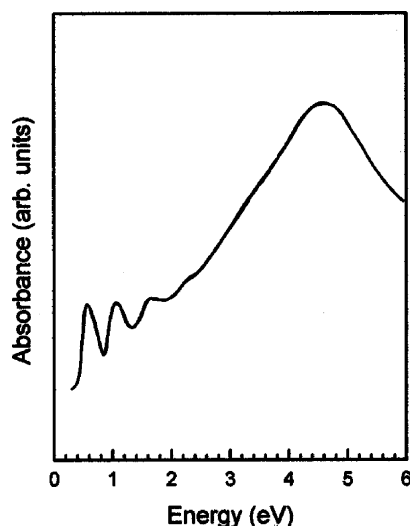
Fig. 14. Optical absorption of purified SWNT thin film samples synthesized by the arc-discharge method using a NiY catalyst (after [48]).

Recently, an extensive ab initio local-density-functional study of the electronic dispersion in chiral and achiral isolated and bundled SWNTs was reported [50]. The curvature of the nanotubes was found to reduce the band gap by hybridization and to alter the electronic states responsible for the optical transitions. Even for wide nanotubes ($D = 1.0$–1.5 nm) the energy-levels shift was ~0.1 eV. Bundling of the nanotubes resulted in a further decrease of the energy gap in semiconducting tubes. The (10, 0) bundle was found to be metallic. It is concluded that the obtained intertube dispersion of ~0.1 eV could broaden the electronic density of states and the optical absorption bands in bundles.

4.4. Optical absorption

In Fig. 14, the optical absorption spectrum of purified SWNT thin films measured by Kataura et al. [48] is presented. The three peaks at 0.68, 1.2 and 1.7 eV were found to correspond to the DOS peaks of two semiconducting and one metallic tubes. Additionally, the large absorption band at 4.5 eV was ascribed to the π-plasmon of SWNTs observed also in the energy-loss spectrum. On doping with electron donors (K, Cs) or acceptors (Br_2, I_2), the absorption bands of SWNTs are smoothed and completely vanish at high doping level ($x > 0.04$) [51]. This phenomenon is explained by charge transfer from the donors to the nanotubes, filling up the lowest unoccupied bands and depleting the absorption bands. In a similar way, the acceptors lead to depletion of absorption bands. Hwang et al. [52] measured the reflectance of an unaligned mat of SWNTs in the range 0.003–3 eV. The reflectance spectrum exhibited peaks at 0.7, 1.3, 1.9, and 2.6 eV ascribed to transitions between the DOS peaks of semiconducting and metallic nanotubes. The polarized absorption of a freestanding SWNT fiber showed considerable anisotropy with bands at 1.9 and 2.6 eV being strongly polarized in parallel direction.

Li et al. [53] reported the polarized optical absorption spectra of single-walled 4 Å nanotubes in the channels of an $AlPO_4$–5 single crystal. The spectra in parallel polarization of the incident light, bands at 1.37, 2.1 and 3.1 eV were observed (Fig. 15). These peaks were assigned to dipole transitions between the van Hove singularities of tubes (5, 0), (3, 3), and (4, 2). In cross polarization
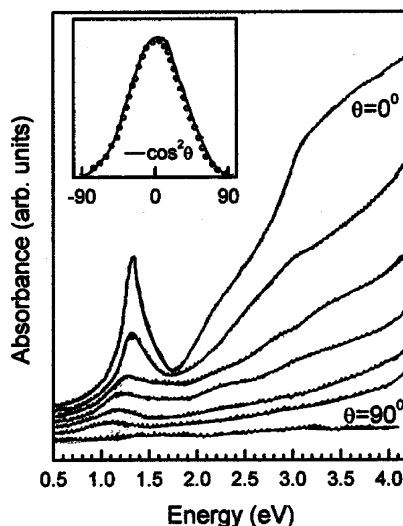
Fig. 15. The polarized optical absorption spectra of the SWNTs in the channels of $AlPO_4-5$ crystal for different angle θ of the light polarization with respect to the tube axis (after [53]).

the nanotube were nearly transparent in the measured region 0.5–4.1 eV. The absence of peaks in this case was ascribed to depolarization effects [46]. This conclusion is in accord with estimation of the polarizability of nanotubes [54], where the local field corrections, accounting for the depolarization effects, lead to vanishingly small polarizability in the direction perpendicular to the tube axis.

Recently, a detailed analysis of the optical properties of SWNTs with different mean diameters as produced by laser-ablation was reported [55]. It was possible to accurately determine the mean diameter and diameter distribution in bulk SWNT samples from a combined study of optical absorption, high-resolution electron energy-loss spectroscopy (EELS) in transmission and tight-binding calculations (Fig. 16). The optical response could be well described assuming a Gaussian distribution of nanotube diameters and the predicted inverse proportionality between the nanotube diameter and the energy of the absorption features. The obtained mean diameters and diameter distributions were in very good agreement with the values derived from other bulk sensitive methods such as electron diffraction, X-ray diffraction, and Raman scattering.

4.5. Low-energy–loss measurements

In the low-energy electron energy-loss spectroscopy performable within a transmission electron microscope low-energy electrons are scattered by the solid ejecting valence electrons into the unoccupied states. The measured quantity is the loss function, which is the probability for the electron to lose certain energy per unit length. The loss spectra reflect the joint density of states between the occupied and unoccupied states. The high-energy particles, bombarding the solids, can travel ~ 0.1 μm inside the solid and, therefore, this technique is not surface sensitive.

Pichler et al. [56] measured the loss function $Im(-1/\varepsilon(\omega, q))$ of purified SWNTs for various momentum transfers q and low excitation energies ($\varepsilon(\omega, q)$ is the dielectric function). The spectra show peaks corresponding to excitation from the valence bands to the conduction bands as well as plasmon peaks (Fig. 17). The latter are at 5.2 eV (π-plasmon) and 21.3 eV ($\pi + \sigma$-plasmon), somewhat lower compared to the corresponding values for graphite (6 and 27 eV) because of
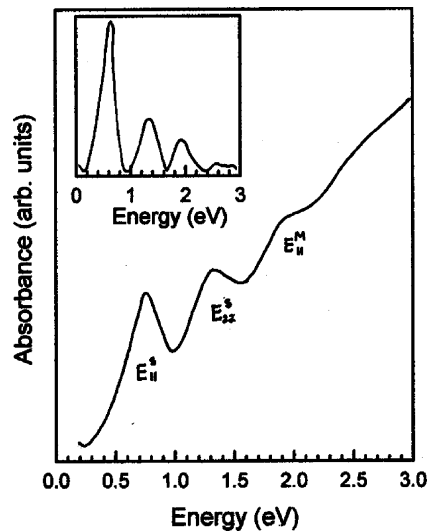
Fig. 16. Measured optical absorbance between 0 and 3 eV of SWNT samples with 1.3 nm mean diameter. E_{11}^S, E_{22}^S, and E_{11}^M are the lowest interband transitions in semiconducting (S) and metallic (M) SWNTs (inset: same after subtraction of the large π-plasmon contribution) (after [55]).

curvature effects in nanotubes. The π- and π + σ-plasmons show strong dispersion (dependence on the wavevector q) (Fig. 18). The peaks observed at 0.85, 1.45, 2.0 and 2.55 eV are dispersionless and can be attributed to π–π* interband transitions of different nanotubes. For dipole transitions, these energies are equal to the separation between the mirror spikes of the electronic DOS. Using theoretical predictions for the electronic band structure of the nanotubes, the observed peaks can be assigned to nanotubes with certain diameters and chiralities [48].

Kociak et al. [57] measured the EELS spectra of isolated MWNTs in a near-perpendicular geometry of the electron beam with respect to the tube axis. The EELS spectra recorded by scanning the probe perpendicular to the nanotube axis π- and π + σ-bulk plasmon peaks are observed. In all
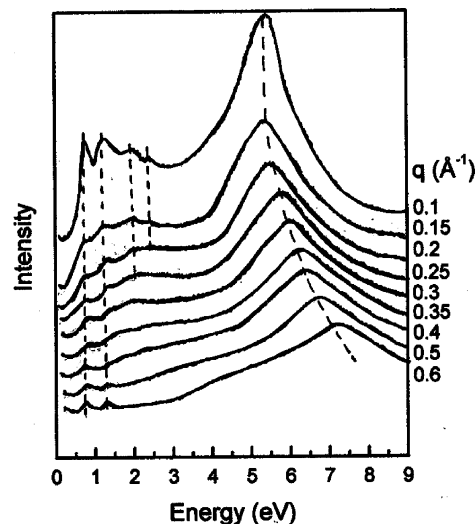

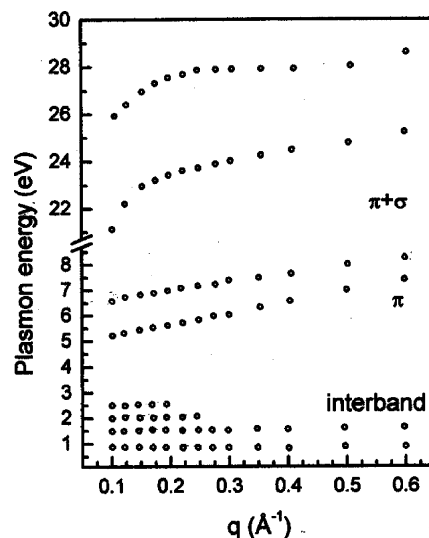Fig. 17. Low-energy EELS spectra exhibiting peaks due to interband transitions and plasmons (after [56]).

Fig. 18. Energy dispersion of the peaks in the low-loss spectra of SWNTs (after [56]).

spectra, the π-plasmon peak remained near 6 eV. The π + σ-plasmon shifted from 27 eV (graphite-like) near the nanotube center to about 23 eV near the nanotube edge. This shift is interpreted as a geometrical effect due to the change of the relative orientation of the tube layers with respect to the electron beam during the scan. The limiting values correspond to parallel and perpendicular orientation of the beam and can be associated with the corresponding bulk plasmons in graphite. The EELS spectra recorded by scanning the probe without crossing the nanotube surface plasmon peaks are observed at 6, 14, and 17–18 eV.

5. Electrical transport in perfect nanotubes

Electrical transport through carbon nanotubes has attracted considerable interest due to the many possible applications of the nanotubes in nanoscale electronic devices. The nanotubes are nearly perfect 1D conductors in which at low temperatures a number of interesting mesoscopic phenomena has been observed such as single-electron charging, resonant tunneling through discrete energy levels and proximity-induced superconductivity. At relatively high temperatures, tunneling conductance into the nanotubes displays power-law suppression as a function of temperature and bias voltage, which is consistent with the physics of the 1D Luttinger liquid. The main scattering mechanism in metallic tubes is due to optical or zone-boundary phonons. The scattering and coherent-backscattering processes lead to new phenomena at low temperatures. The transport experiments involved both two- and four-probe measurements on individual MWNTs [58–60], SWNT bundles [61,62], and isolated SWNTs [63].

In the first electrical resistance measurements of an individual MWNT down to $T = 20$ mK by Langer et al. [58], in zero magnetic field a logarithmic decrease of the conductance with decreasing temperature and saturation below $T \approx 0.3$ K were observed. In the presence of a magnetic field, perpendicular to the tube axis, a pronounced and positive magnetoresistance was measured. The temperature dependence of the conductance in a magnetic field was found consistent with 2D weak localization.
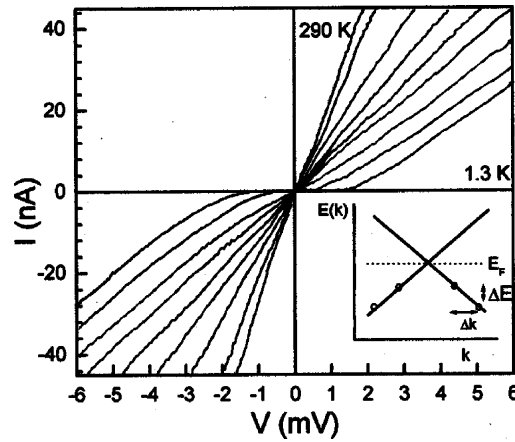
Fig. 19. The *I–V* characteristics of a 12 nm-diameter bundle of about 60 SWNTs is measured using a four-probe method. The right inset shows the band structure of a metallic tube near the band crossing point at the Fermi level. The dots designate the quantized energy levels (after [61]).

5.1. Electrical transport in bundles of SWNTs

Bockrath et al. [61] measured electrical transport through bundles of SWNTs bridging contacts separated by 200–500 nm (Fig. 19, left inset). Four-probe method was used with contacts lithographically defined over the bundles. The *I–V* characteristics exhibits strong suppression of the conductance near $V = 0$ for $T < 10$ K (Fig. 19). The linear-response conductance G of the bundle as a function of the gate voltage V_g (Fig. 20) consists of a series of peaks separated by regions of very-low conductance. The peak width increases linearly with the temperature T as an indication that transport takes place via resonant tunneling through discrete energy levels and the electronic wavefunctions are extended between the contacts, i.e., the nanotubes behave as coherent nanowires at mK temperatures. The peak structure is not observable above $T = 50$ K.

The conductance shows complex step-like dependence on the gate voltage V_g, which can be understood in terms of Coulomb blockade transport in quantum wires and dots considering the nanotube as an extended quantum dot (Fig. 20). The period of the peaks in the gate voltage ΔV_g is
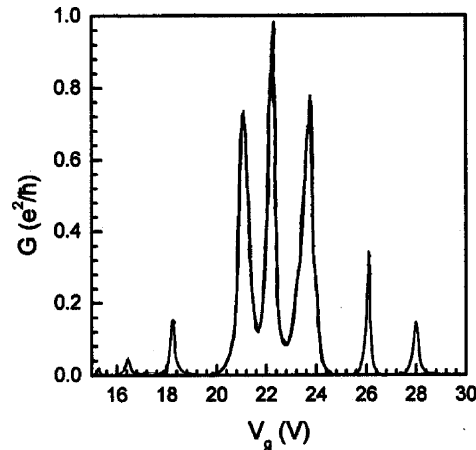

Fig. 20. Conductance G vs. gate voltage V_g at $T = 1.3$ K. The peak spacing is typically ∼1.5 V (after [61]).
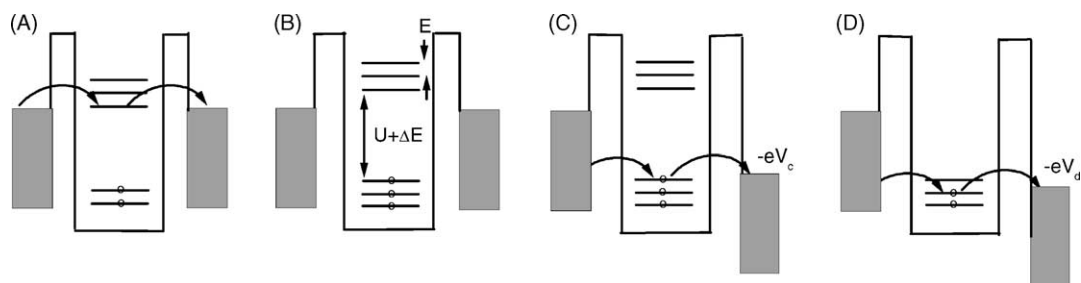
Fig. 21. (A–D) Schematic energy-level diagrams for the nanotube with the two leads with the Coulomb blockade model (after [61]).

determined by the energy for adding an additional electron to the dot. In the simplest model which takes into account the Coulomb interactions and energy-level quantization, the peak spacing is $\Delta V_g = (U + \Delta E)/e\alpha$. Here $U = e^2/C$ is the Coulomb charging energy for adding an electron to the dot, ΔE is the single-particle energy spacing, $\alpha = C_g/C$, C is the total capacitance of the dot, C_g is the capacitance between the dot and the back gate. At gate voltages, corresponding to a peak in Fig. 20, an empty level aligns with the electrochemical potential in the leads and single electrons can tunnel on and off the dot at $V = 0$ (Fig. 21A). At gate voltages in between the peaks, tunneling is suppressed because of the single-electron charging energy U, which is the energy for adding an electron to the dot (Fig. 21B). However, if V is increased so that the electrochemical potential of the right lead is pulled below the energy level of the highest filled state, an electron can tunnel off the dot resulting in an increase in G (Fig. 21C). Further increasing V allows tunneling out additional states, giving additional increase in G (Fig. 21D). This Coulomb blockade model was applied to estimate the energy-level spacing ΔE and the charging energy U. It was obtained that $\Delta E \sim 0.5$ eV/L (nm) and $U \sim 14$ eV/L (nm), where L is the nanotube length. The peaks in the conductance G approach the theoretical maximum of e^2/h for single-electron transport. The deviation from this value means that the barriers at the leads are not equal and suggests the presence of disorder along a filamentary pathway, which could break it into weakly coupled localized regions.

5.2. Electrical transport in individual SWNTs

Measurements of the conductance of individual SWNTs using two-probe method were performed by Tans et al. [63]. In these measurements, the nanotubes were metallic with resistance of tens of kiloohms and formed a tunnel barrier of high resistance of $\sim$1 MΩ with the electrodes. The I–V curves (Fig. 22) showed a clear gap around zero bias voltage. For higher voltages, the current increases in steps. The gap appears to be suppressed for certain gate voltages V_g and has a maximum value in between. The variation of the gap with V_g around zero bias voltage V implies Coulomb charging of the tube. This phenomenon occurs in metallic nanotubes when the contact resistance is much larger than nanotube resistance and when the capacitance C of the object is so small that adding a single electron costs a significant charging energy $U = e^2/2C$. At low temperatures ($U \gg k_B T$) the current is blocked and will flow only when $eV > U$. The increase of V will result in increasing the number of levels within the bias window and in a characteristic Coulomb staircase behavior of the I–V curves. Such behavior cannot be observed in bundles of SWNTs because the energy-level spacing ΔE there is much lower than for individual SWNTs. It was estimated that $\Delta E \sim 0.4$ eV and $U \sim 2.6$ eV.
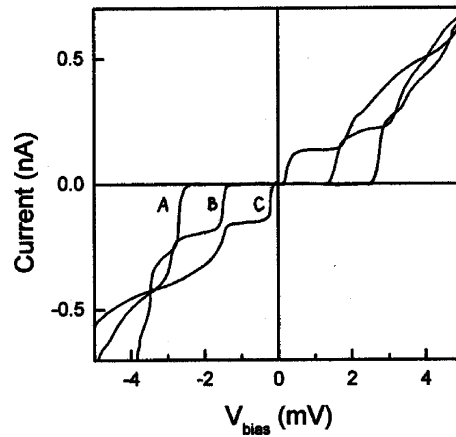
Fig. 22. *I–V* curves of the SWNT at different gate voltages V_g. The inset shows more such curves. The step-like increase of the current at higher voltages may result from an increasing number of excited states entering in the bias window (after [63]).

At high temperatures where the Coulomb blockade is unimportant, tunneling into a metallic nanotube is consistent with predictions for tunneling into a Luttinger liquid, which is formed due to strong electron interactions [64]. As a result, the electrons form a correlated ground state called Luttinger liquid, which is characterized by low-energy charge and spin excitations. The Luttinger parameter *g*, describing the strength of the electron interactions, was estimated as $g \approx 0.2$ compared to $g = 1$ for Fermi liquid [65]. The tunneling density of states is suppressed as a power-law function of energy $\rho(E) \sim |E - E_F|\alpha$, where $\alpha \approx 0.4$ for a nanotube and $\alpha = 0$ for a Fermi liquid. The resulting tunneling current should be suppressed with $dI/dV \sim V^\alpha$, and the linear conductance $G(T) \sim T^\alpha$ vanishes with temperature. The measurements of the linear conductance and the differential conductance of bundles of SWNTs as a function of temperature and voltage were found to agree with the predictions for tunneling into a Lattinger liquid [66].

At low enough temperature *T*, the linear conductance vs. gate voltage shows characteristic Coulomb oscillations, occurring each time when an electron is added to the nanotube within the bundle. For $T > 20$ K, the thermal energy exceeds the charging energy, which results in complete disappearance of the Coulomb oscillations and conductance, nearly independent of the gate voltage. The temperature dependence of the conductance *G* showed approximate power-law behavior $G(T) \sim T^\alpha$ with $\alpha \approx 0.3$ to 0.6 (Fig. 23). In the low-bias (linear-response) regime, d*I*/d*V* is a (temperature-dependent) constant. At high biases, d*I*/d*V* increases with increasing bias voltage *V* (Fig. 24) described by a power law $dI/dV \sim V^\alpha$. The curves of d*I*/d*V* at different *T* can fall into one curve by plotting the scaled conductance $(dI/dV)/T^\alpha$ against $eV/k_B T$.

An intrinsic large bias transport property of individual metallic single-walled nanotubes was measured using low-resistance electrical contacts [67]. For low bias voltage, d*I*/d*V* could be fit with a power-law function. When bias was increased up to 5 V, the current saturated with current density exceeding 10^9 A/cm^2 (Fig. 25). The resistance $R = V/I$ could be fit well by a simple linear function of *V*: $R = R_0 + V/I_0$, where R_0 and I_0 are constants ($I_0 = 25$ μA). The *R*(*V*) dependence was explained by backscattering of electrons from optical or zone-boundary phonons which gives rise to a mean free path scaling inversely with *V*. The band structure of a metallic nanotube contains two propagating 1D subbands near the Fermi energy. In the absence of scattering, the chemical potential of the right and left moving states will differ by the applied voltage *eV*. At low voltage this leads to an Ohmic response. With the increase of *V*, a steady state is established, in which the (say) right
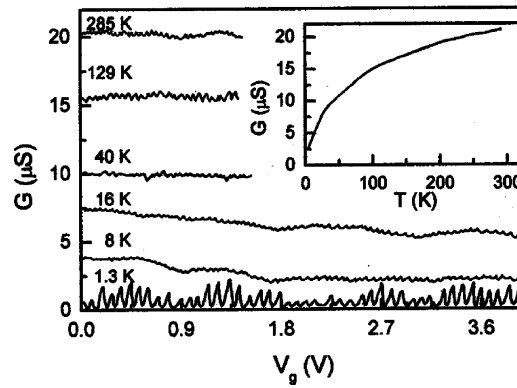
Fig. 23. Two-probe linear conductance vs. gate voltage at several different temperatures T (after [66]). Coulomb blockade behavior is observed at low temperatures while the conductance is nearly independent of gate voltage at $T > 20$ K.

Fig. 24. Scaled conductance vs. eV/kT (after [66]).

Fig. 25. The I–V characteristics at different temperatures measured using low-resistance contacts. The inset shows the resistance $R = V/I$ vs. bias voltage V (after [67]).

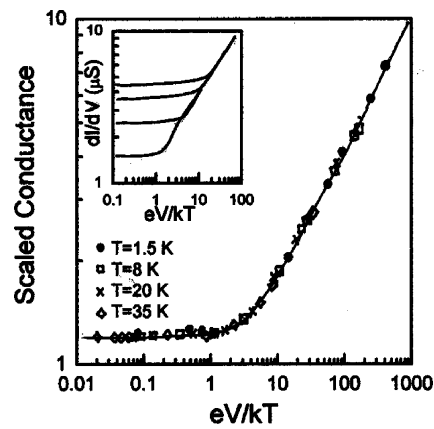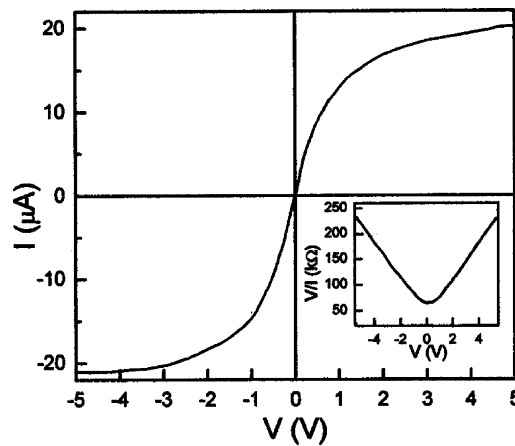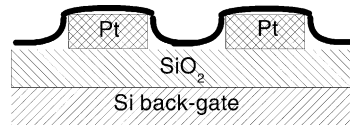Fig. 26. Schematic side view of a nanotube-base FET (TUBEFET) device. A single semiconducting nanotube is contacted by two electrodes on a SiO_2 layer over a Si substrate (after [68]).

moving electrons are populated to an energy $h\Omega$ higher than the left moving ones. Assuming strong electron–phonon coupling, the high-energy electrons are backscattered by emitting optical or zone-boundary phonons of energy $h\Omega$. This mechanism leads to a saturation current $I_0 = (4e/h)h\Omega$. For a typical phonon energy of $h\Omega = 0.16$ eV, the saturation current is found to be $I_0 = 25$ μA, the same as the experimentally derived value.

5.3. Nanotube field-effect transistors

Transport measurements on semiconducting nanotubes have shown that a nanotube connected to two metal electrodes has the characteristics of a field-effect transistor (Fig. 26). By applying voltage to a gate electrode, the nanotube can be switched from a conducting to an insulating state. Such a system was shown to be operative even at room temperatures thus meeting the important requirement for potential practical application [68]. A typical *I–V* characteristics of a nanotube FET (Fig. 27) shows that by changing the gate voltage from positive to negative, the curve is changed from highly non-linear insulating behavior with a large-gap to linear metallic behavior. The FET operation was explained by the semiclassical band-bending models currently used for traditional semiconductor devices.

Martel et al. [69] fabricated field-effect transistor based on individual single- and multi-walled carbon nanotubes. The FET consisted of nanotubes bridging two Au electrodes deposited on a 140 nm thick SiO_2 oxide film on a doped Si wafer, which was used as a back gate. The electrodes were defined using electron beam lithography. The source–drain current I through the nanotubes was measured at room temperature as a function of the bias voltage V and the gate voltage V_g. For a SWNT FET, for $V_g < 0$, the *I–V* curves were linear whereas for $V_g \gg 0$ they became increasingly
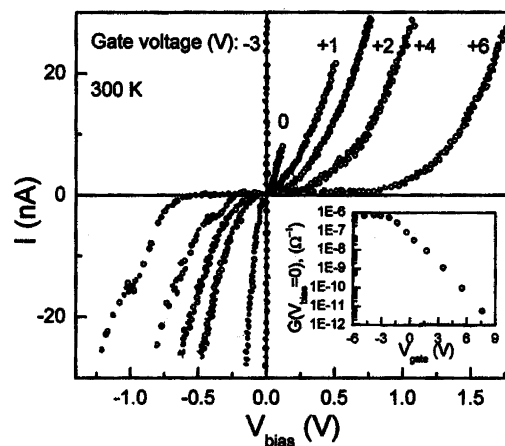

Fig. 27. The *I–V* characteristics of a nanotube FET for various values of the gate voltage V_g (after [68]). A negative V_g leads to ohmic behavior while a positive V_g results in a strong suppression of the current at low bias voltage V and non-linear *I–V* curves at higher bias.

non-linear. The current I decreased on increase of V_g, which showed that the device operates as a FET but also that transport through semiconducting SWNTs was dominated by holes. The *I–V* curves saturated for $V_g < 0$. The conduction modulation exceeded five orders of magnitude. The behavior of the *I–V* curves versus V_g was similar to that of a p-channel metal-oxide–semiconductor FET. The MWNT FET showed no gate effect.

Recently, the realization of room-temperature single-electron transistors within individual metallic SWNTs was reported Postma et al. [70]. The device consists of a metallic island connected by tunnel barriers to two metallic leads. For temperatures and bias voltages that are low relative to a characteristic energy required to add an electron to the tube, electrical transport through the device is blocked. Conduction can be restored by gate voltage turning the device into a three-terminal transistor. The island is formed by two strong bends within a metallic nanotube. The differential conductance dI/dV versus gate voltage V_g shows a 0.2 V wide gap opening and closing in a periodic manner with V_g. In a similar way, the bias voltage V can be used to modulate the conductance. These characteristics show Coulomb blockade at room temperature. It is shown that the addition energy is much larger than the thermal energy at room temperature, which explains the room-temperature operation of the device. At temperature $T = 30$ K, the dI/dV curve shows step-like behavior due to the shifting up the energy levels of the island with the bias, which makes them available for electrical transport and leading to increase in current. The peak conductance G varies with temperature T as $T^{0.68}$. This behavior cannot be explained with the model of Luttinger island connected by tunnel barrier to two semi-infinite Luttinger liquids, where one obtains $G \sim T^{-0.2}$. Another mechanism was proposed, in which the electrons tunnel coherently from the end of one nanotube to the end of the other nanotube lead through a quantum state in the island. This emphasizes the critical role of disorder or impurities on the transport characteristics of single-electron transistors. Because semiconducting nanotubes are, unlike metallic tubes, prone to disorder and unintentional doping, molecular devices based on metallic tubes are preferred.

SWNTs-based field-effect transistors can be used in logic circuits as demonstrated by Bachtold et al. [15]. The transistors showed favorable device characteristics such as high gain (>10), a large on-off ratio (>10^5), and room-temperature operation. The one-, two, and three-transistor circuits exhibited a range of digital logic operations, such as an inverter, a logic NOR, a static random-access memory cell, and an ac ring oscillator.

6. Electrical transport through junctions

Due to the sensitivity of the electronic properties of carbon nanotubes on their structure, they are suitable for preparation of metal–semiconductor, semiconductor–semiconductor and metal–metal junctions. They can be realized as on-tube junctions by joining together seamlessly two tubes of different chirality [71]. It has been demonstrated that the introduction of pentagon–heptagon pair of defects into the hexagonal network of a carbon nanotube can change the chirality of the tube and change its electronic properties [72–75]. Another way to realize an on-tube junction is by chemical doping of segments of the nanotube [76]. Nanotube junctions can be constructed from Y-branched nanotubes [77] or from crossed nanotubes [78]. It has been demonstrated that the nanotube junctions can be used successfully as building elements of nanoscale devices.

6.1. On-tube junctions

A tight-binding method was used to calculate the change in the electronic structure of a single-walled carbon nanotube arising from the introduction of a pentagon–heptagon pair of defects in the
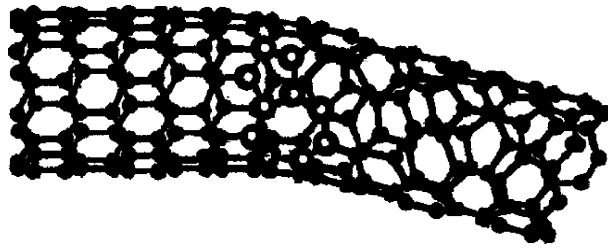
Fig. 28. Atomic structure of a (8, 0)/(7, 1) nanotube with a pentagon–heptagon pair (light gray balls) (after [73]).

hexagonal network of the tube by Chico et al. [73]. A semiconducting nanotube (8, 0) can be matched to a metallic nanotube (7, 1) by means of a single pentagon–heptagon pair of defects (Fig. 28). The resulting structure is a metal–semiconductor (Schottky) barrier. Analogously, a semiconductor–semiconductor junction can be formed by connecting nanotubes (8, 0) and (5, 3) by adding three pentagon–heptagon pairs. In both cases, the calculated local density of electronic states averaged over a unit cell, swiftly changes from that of the first tube to that of the second tube in a few unit cells distance along the junction. More generally, a single pentagon–heptagon pair with symmetry non-parallel to the tube axis changes the chirality of a nanotube by one unit from (n, m) to $(n + 1, m − 1)$ or $(n − 1, m + 1)$.

The observation of non-linear junction-like behavior in ropes of SWNTs was reported by Collins et al. [79]. The tip of a scanning tunneling microscope was used as a manipulator to retract the end of a rope from the sample and measure the I–V characteristics at different length along the rope. With the increase of the length the measured I–V curve remained non-linear but symmetric while beyond length of 2 μm the curve became non-linear asymmetric (Fig. 29). The latter behavior was discussed in the terms of present defects, e.g., pentagon–heptagon pairs that change the electronic properties of the tubes.
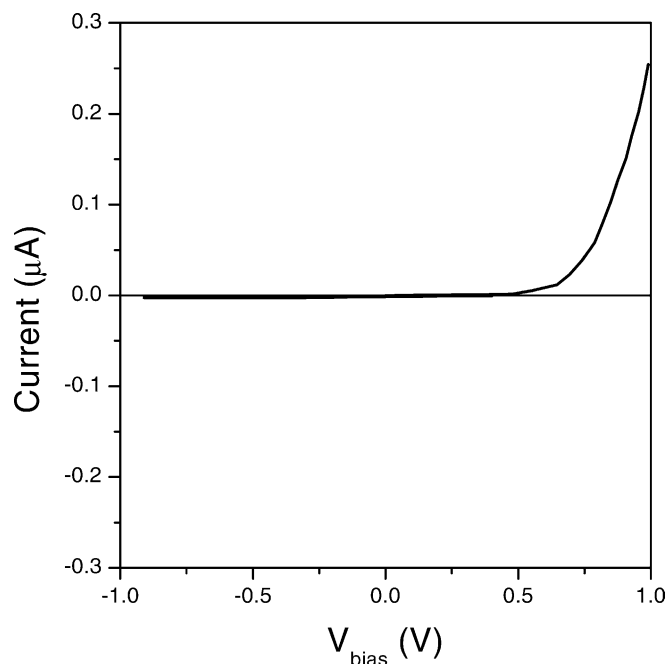

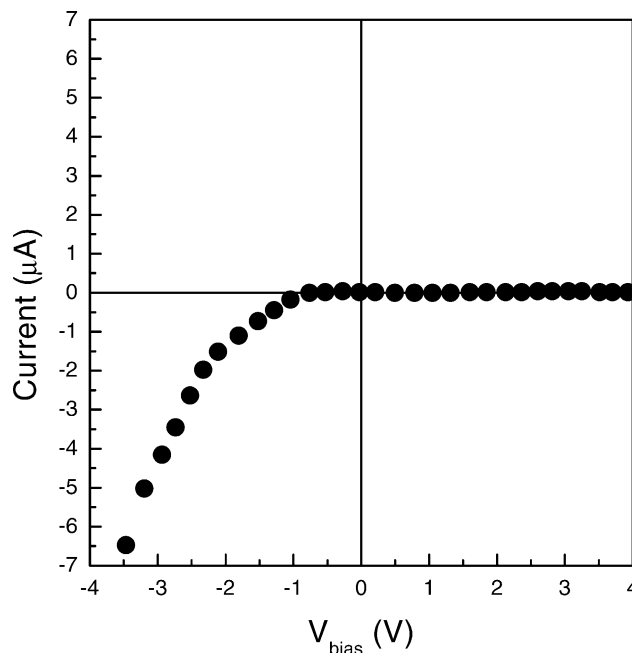Fig. 29. I–V curve of a rope of SWNTs measured using a scanning tunneling microscope (after [79]).

Fig. 30. I–V curve for an individual Y-junction nanotube (after [77]).

Electrical transport measurements through a nanotube consisting of straight segments connected by a sharp kink of about 40° were reported by Yao et al. [80]. It is argued that the kink is due to a pentagon–heptagon pair of defects placed on the opposite sides of the kink. The I–V curve is similar to that in Fig. 30 indicating that one of the straight segments is metallic and the other is semiconducting, so that the kink is an metal–semiconductor heterojunction acting as a rectifying diode. Another one of the measured nanotubes had similar geometry as the former but with metallic straight segments the kink being a metal–metal junction. The linear-response conductance G across the junction showed power dependence on temperature T: $G \sim T^{\alpha}$, which was interpreted as a signature for strong electron–electron correlations and Luttinger liquid behavior of the electrons. The Luttinger parameter g for the straight segments is estimated as $g \approx 0.22$. It was supposed that the conduction process across the junction took place via end-to-end tunneling between the two Luttinger liquids. In this case, the power-law exponent can be derived as $\alpha = (g^{-1} - 1)/2 = 1.8$ which compares well with the experimental value of 2.2. The I–V characteristics across the metal–metal junction are non-linear at all temperatures and can provide independent verification of the Luttinger liquid theory. In this case, the current is expected to increase as $V^{\alpha+1}$ for $eV \gg k_{B}T$. The experimental exponent was obtained as 2.1, which is very close to the value of 2.2 for the G–T curve.

Another way to realize an on-tube junction is by modulated chemical doping of individual nanotubes [76]. Prior to doping, the nanotubes behave as a p-type semiconductor due to adsorbed molecules, chemical groups on substrates, or charge transfer with metal electrodes. Doping half of the nanotube with potassium allows converting it from p- to n-type and obtaining an on-tube p–n junction. The electron and hole concentrations can further be controlled by the gate. Several regimes are observed at different gate voltages: rectifying behavior, negative differential conductance due to tunneling of electrons across degenerately-doped junction, and Coulomb blockade at low temperature.
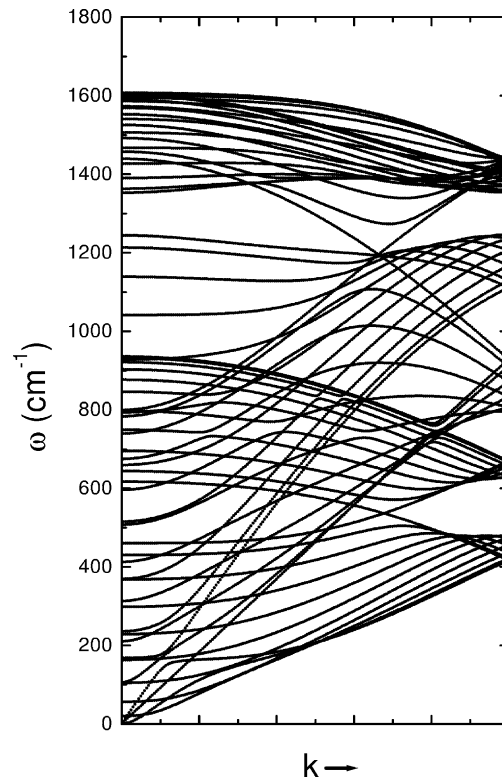
Fig. 31. (a) The calculated phonon dispersion of a SWNT (10, 10). There are four acoustic branches: longitudinal, twist, and two transverse ones. The latter two depend quadratically on the wavevector near the Brillouin zone centre.

6.2. Y-junctions and crossed junctions

Papapdopoulos et al. [77] studied electronic transport in Y-junction carbon nanotubes. The Y-junctions were produced by CVD growth in branched nanochannel alumina templates [81]. The method produces multi-walled nanotubes in aligned arrays with adjustable "stem" and "branch" diameters. The electrical transport measurements were performed both on arrays and individual Y-juctions. The Y-junctions were typically 6–10 μm in total length with stem/branch diameters of ~50/35 and 60/40 were used. Array densities were 10^{10} cm^{-2}. The measurements on individual nanotubes showed non-linear and asymmetric *I–V* behavior (Fig. 31). Similar behavior had arrays of ~10^2–10^8 Y-junctions. Because the CVD method produces p-doped semiconducting multi-walled nanotubes, the rectifying property of Y-junctions was modeled as a p–p isotype semiconductor heterojunction using standard heterostructure methods. It is suggested that a three-terminal nanoscale transistor can be realized by applying different voltages to each of the Y-junction branches.

Fuhrer et al. [78] fabricated junctions consisting of two crossed SWNTs with electrical contacts at each end of each nanotube. The individual nanotubes were metallic (M) or semiconducting (S) and formed MM, MS, and SS four-terminal devices. While the *I–V* curves for the MM and SS junctions showed linear behavior, the curves for the MS junctions had non-linear behavior characteristic of a Schottky barrier between a metal and a p-type semiconductor. In the latter case for reverse bias, there is a measurable current due to the small depletion region leading to tunneling through the barrier. It is

argued that a three-terminal device solves this problem and opens the ways for constructing good rectifiers from narrow Schottky barriers.

7. Vibrational properties

The atomic vibrations in carbon nanotube were studied theoretically within force-constant models in the zone-folding approximation [82] or for the concrete nanotube structure [83–85], within tight-binding models [86–89] and ab initio models [90–92]. The experimental measurement of the vibrational eigenfrequencies is performed mainly by resonant Raman scattering of light when the laser light energy is close to the energy of allowed electronic transitions. Since the resonance conditions are different for different nanotube types, the Raman spectroscopy allows identifying the possible nanotubes present in the nanotube samples. Recently, Raman measurements have been performed with parallel-polarized light on individual MWNTs [93], and SWNTs [94–96], and with cross-polarized light on individual SWNTs [97].

7.1. Phonon dispersion

The phonon dispersion of rolled-up SWNTs can be obtained within a force-constant model fitted to inelastic neutron scattering, Raman scattering and infrared absorption data on graphite and by using the zone-folding approximation [98,99,82]. In this approximation the phonon dispersion $\omega_{k\mu}$ of a given nanotube is obtained from the phonon dispersion $\omega_{2D}(\boldsymbol{k})$ of the graphene sheet by folding it along a certain direction in the 2D Brillouin zone of graphene. Explicitly, the zone-folding is expressed by the relation

$$\omega_{k\mu} = \omega_{2D}\left(k\frac{\boldsymbol{K}_2}{|\boldsymbol{K}_2|} + \mu\boldsymbol{K}_1\right),$$

where k is the 1D wavevector of the nanotube ($-\pi/T < k < \pi/T$) and μ is the discrete quantum number ($\mu = 1, 2,\ldots, N$). The vectors $\boldsymbol{K}_1$ and $\boldsymbol{K}_2$ are expressed through the reciprocal lattice vectors $\boldsymbol{b}_1$ and $\boldsymbol{b}_2$ of the graphite sheet (see Section 4).

The zone-folding approximation has two shortcomings concerning the $k = 0$ acoustic phonons. First, in the graphene sheet there are two translational phonons with in-plane atomic displacements and one translational phonon with out-of-plane atomic displacements. Upon rolling the sheet into a cylinder, the translational phonon with perpendicular to the plane displacements will correspond to a breathing mode, in which all atoms vibrate uniformly along the radial direction, the so-called radial-breathing mode (RBM). The RBM has non-zero frequency, which cannot be reproduced by zone-folding and has to be calculated analytically. The estimations show that the RBM frequency ω is linear in the tube radius R: $\omega(R) = C/R$ with C being a constant. Secondly, the two $k = 0$ acoustic phonons of a tube with translational atomic displacement perpendicular to the tube axis are not eigenmodes of the graphite sheet. To obtain these two modes by zone-folding, a perturbation has to be added to the dynamical matrix. Finally, the effect of curvature on the force constants is neglected in the zone-folding approximation implying that the hybridization between the sp^2 and p_z orbitals is small. Estimations based on using the semi-empirical interatomic Tersoff potential show that the tube curvature has negligible effect on the mode frequencies for tubes of diameter larger than ~1 nm [100]. The mentioned shortcomings of the zone-folding approximation are partly removed in a force-constant model that accounts for the nanotube structure [83]. This model predicts that the acoustic

branches are linear in k near the Brillouin zone center while the transverse elastic waves in thin rods are quadratic in k and so should be the transverse acoustic (TA) phonons in nanotubes. The use of valence force fields that account for many-body interatomic interactions allows reproducing this quadratic dependence of the transverse acoustic waves in nanotubes [101] (see Fig. 31). The direct calculations of the phonons in nanotubes are usually based on non-optimized or optimized nanotube structures. The use of empirical force-constant models does not allow for structural optimization and predefined structures have to be used [83–85]. The nanotube structure can be optimized within tight-binding models [86–89] and ab initio models [90–92].

Among the various phonons, of greatest importance for the sample characterization are the RBM and the so-called G-band modes because they are observable in the Raman and infrared spectra. The G-band consists of in-plane bond-stretching modes, which originate from the E_{2g} in-plane stretching mode in graphene. In nanotubes, due to symmetry-breaking effects associated with the nanotube curvature, this E_{2g} mode gives rise to six Raman-active modes ($2A_1 + 2E_1 + 2E_2$) in chiral tubes and to three Raman-active modes ($A_{1g} + E_{1g} + E_{2g}$) in armchair and zigzag tubes. The force-constant models usually use insufficient number of force constants, which does not allow for precise reproduction of the overbending of the highest optical branch of graphene [83–85]. Even using force constants, precisely fitted to the phonon dispersion of graphene, the force-constant models will not be able to reproduce correctly the splitting between these modes because of the partial description of the curvature effects. The tight-binding models have the drawback yielding usually by ~10% too high frequencies of the G-band modes [86–89]. Only ab initio models can predict fairly well the G-band modes [90–92].

7.2. Raman spectroscopy

In the first years of the nanotube research, only samples consisting of tangled SWNTs, ropes of SWNTs or MWNTs were measured by Raman scattering of light. The Raman spectra exhibited mainly three bands: the RBM band at ~200 cm^{-1}, the G-band due to in-plane bond-stretching modes at ~1600 cm^{-1}, and a weak disorder band (D-band) at ~1350 cm^{-1} [7]. When ropes of SWNTs with uniform diameters were produced by laser evaporation, it became possible to perform more rigorous analysis of the structure of the RBM and the G-bands [88] (Fig. 32). The abrupt increase of the peak intensity for certain laser excitation energies was explained by resonant scattering, which takes place when the incident or scattered photon energy is equal to the energy E_{cv} of an allowed electronic transition between valence and conduction bands for a given SWNT. Theoretical predictions for the dependence of the transition energies on the nanotube diameter were used to narrow the possible nanotube types in the sample. The precise determination of the nanotube types in the sample was accomplished by assignment of the peaks in the low-frequency Raman bands to RBMs by use of the theoretical dependence of the RBM frequency ω on the tube radius R: $\omega(R) = C/R$. Recently, this power law with $C = 124$ cm^{-1}nm was used for precise (n, m) determination of isolated SWNTs by resonant Raman scattering [102]. A slightly different value $C = 111.875$ cm^{-1} nm was used for chirality assignment of the internal tubes of double-walled carbon nanotubes [103]. G-band splitting was observed in experiments on individual MWNTs as well [104]. Since the nanotube samples usually consist of nanotubes of different radius and chirality, the Raman spectra contain information about the nanotube diameters and chirality. This determines the role of the resonant Raman spectroscopy as an important tool for the structural characterization of the nanotubes.

The unambiguous characterization of the nanotubes can be done only by means of polarized Raman measurements. For a chiral nanotube, the Raman-active modes have the following activity:
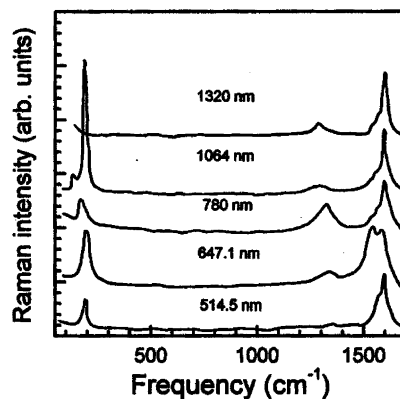
Fig. 32. Room temperature Raman spectra for ropes of SWNTs at five different laser excitation energies. The excitation energy, the power density and the peak positions are indicated (after [88]).

A_1(ZZ, XX), E_1(ZX, XZ), E_2(XX), where Z is along the tube axis and X is perpendicular to it. Choosing different light polarization, the separate peaks due to A_1, E_1, and E_2 modes can be identified. Recently, polarization measurements on individual SWNTs and MWNTs were performed and detailed analysis of the Raman peaks was attempted: individual MWNTs [93], and SWNTs [94–96]. Jorio et al. [94] obtained polarized Raman spectra from a rope of aligned semiconducting SWNTs. Based on group theory the G-band structure was deconvolved into four components: 1547 cm^{-1} (E_2), 1567 cm^{-1} ($A_1 + E_1$), 1590 cm^{-1} ($A_1 + E_1$) and 1607 cm^{-1} (E_2).

Duesberg et al. [96] performed polarized micro-Raman spectroscopy on individual SWNTs or thin ropes of SWNTs. The angular dependence of the intensities $I(\alpha)$ of the RBM and G-band peaks for both parallel- and cross-polarized configuration was found to be the same and of the form cos$^2(\alpha)$ (α is the angle between the light polarization and the tube axis). In other words, the intensities of all modes are maximal for $\alpha \approx 0°$ and vanish for $\alpha \approx 90°$. This result disagrees with the angular dependence of the non-resonant Raman intensity [83] and implies that the resonant scattering changes this dependence and more generally leads to a breakdown of the selection rules. The vanishing of the intensity for $\alpha \approx 90°$ (the so-called ''antenna'' effect) was attributed to the depolarization effect that reduces strongly the optical response for light polarized perpendicularly to the tube axis [46]. Jorio et al. [105] studied the polarization dependence of the resonance Raman spectra for several different SWNTs. The spectra exhibited strong ''antenna'' effect in all cases. However, contrary to [96], the intensity of the Raman peaks of the RBM and G-band depends on the angle α as cos$^4(\alpha)$ for parallel (VV) configuration and sin$^2(2\alpha)$ for cross (VH) configuration. The resonant scattering for VV configuration was found to lead to a breakdown of the symmetry selection rules, while in VH configuration these rules were still valid. This allowed making the following assignment: 1555 cm^{-1} (E_2), 1566 cm^{-1}, 1592 cm^{-1} (E_1), and 1578 cm^{-1}, 1592 cm^{-1} (A_1). Jorio et al. [97] by use of cross-polarized light obtained resonant Raman spectra of the G-band of SWNTs. Whenever the laser excitation energy was close to optical transition energies $E_{vn} - E_{c(n\pm1)}$, the antenna effect was smeared and a partial breakdown of the selection rules was observed. Therefore, the resonance conditions have to be determined from both types of optical transition: $E_{vn} - E_{cn}$ and $E_{vn} - E_{c(n\pm1)}$.

Due to the resonance character of the Raman scattering in nanotubes, there is still some controversy in the assignment of the G-band peaks. Extensive depolarization ratio study of the G-band modes showed that all peaks in the G-band have A_1 character and the appearance of multiple peaks in the G-band was explained with double resonance processes [106]. By Raman scattering

measurements with cross-polarized light it was shown that some broad features could be explained by double resonance processes but that other features were consistent with single resonance processes [97].

8. Mechanical properties

The carbon nanotubes are expected to have high stiffness and axial strength as a result of the carbon–carbon sp^2 bonding [107]. The practical application of the nanotubes requires the study of the elastic response, the inelastic behavior and buckling, yield strength and fracture. Efforts have been applied to the experimental [108–111] and theoretical [91,101,112–115], investigation of these properties.

8.1. Isolated nanotubes

The linear elastic behavior of individual multi-walled carbon nanotubes was studied by Treacy at al. [108] by measuring the amplitude of the intrinsic vibrations of the nanotubes in the transmission electron microscope. The nanotubes were assumed equivalent to clamped hollow homogeneous cylindrical cantilevers. The mean-square vibration amplitude is linear in temperature with coefficient containing Young's modulus along with the inner and outer radii, and the length of the cantilever. Due to the inevitable experimental uncertainties such as the estimation of the nanotube length, the values of the Young's modulus have a considerable spread. The average value for the Young's modulus was 1.8 TPa, much higher than for typical carbon fibers of 680 GPa [116]. Along with the poor precision, this method has the drawback that the tubes cannot be strained at will. Therefore, this approach cannot evaluate the strength and toughness of nanotubes—properties that are critical to applications. Later, this technique was applied to measure Young's modulus of isolated SWNTs and the average value of 1.25–0.35/+0.45 TPa was obtained [109].

The mechanical properties of SiC nanorods and MWNTs were measured by Wong et al. [110] by use of atomic force microscopy (AFM). The MWNTs were pinned at one end to molybdenum disulfide surfaces by depositing pads of silicon oxide through a shallow mask (Fig. 33). In this method, the AFM tip can be moved perpendicular to the tube and record the lateral force arising from the elastic displacement of the beam by the tip. Large displacements can lead to buckling, plastic deformation or fracture of the nanotube and thereby determine its strength. For small displacements the nanotube can be deformed without damage. In the latter regime, the bending force was measured versus displacement along the unpinned length. These data are used in the equation of
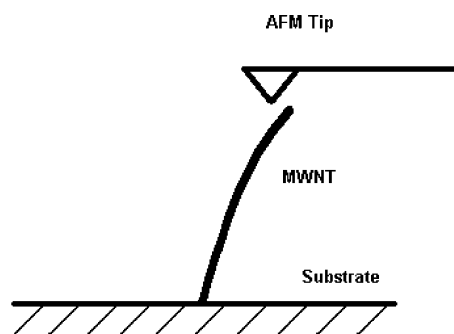

Fig. 33. Schematic representation of the MWNT bending with an AFM tip.

the deflected nanotubes considering them as hollow homogeneous cylindrical cantilevers. The integration of this equation yields the applied force in terms of the Young's modulus and the displacement of the nanotube. The estimated Young's modulus was 1.26 TPa. It was found that nanotube buckle elastically at large deflection angles of $\sim 10°$ for length of 1 µm. The bending strength is defined as the force per unit area at the buckling point because the stiffness drops substantially at this point. The average bending strength was 14.2 ± 8.0 GPa, substantially smaller than for SiC nanorods. The toughness refers to the elastic energy stored by the material before failure. The estimate for a 30 nm diameter nanotube was 100 keV, which is an order of magnitude larger than the strain energy storage in SiC nanorods. Therefore, the ability of nanotubes to elastically sustain loads at large deflection angles enables them to store or absorb considerable energy. Yu et al. [111] used AFM tips to apply tensile load to MWNTs and measured breaking strength of MWNTs between 11 and 63 GPa and Young's modulus between 270 and 950 GPa.

In the theoretical study of the elastic moduli of SWNTs and MWNTs it is assumed that the nanotubes can be modeled as solid or hollow homogeneous cylinders [117]. In most of the calculations, for the case of unilateral stress or shear, the second derivative of the strain energy with respect to the nanotube elongation is calculated to derive the Young's and shear moduli, Y and G. In force-constant model calculations [112] it was obtained that the moduli were insensitive to the tube size and chirality and had the average values $Y = 0.97$ TPa and $G = 0.45$ TPa. In [101], the elastic moduli were derived in a study of the long-wavelength dynamical behavior of the SWNTs and the average values $Y = 55$ eV and $G = 23$ eV were obtained. In several works, molecular-dynamics simulation algorithms using the Tersoff–Brenner potentials for the carbon–carbon interactions were implemented to relax the strained nanotubes and calculate their energy [107,113,114]. For tubes of diameter of 1 nm values of Y of 5.5 TPa [113] and 0.8 TPa [114] were obtained. In a non-orthogonal tight-binding model [115] the average value of the Young's modulus for several chiral and achiral SWNTs of 1.24 TPa was derived. Pseudopotential density-functional theory calculations for a number of SWNTs the average value of Young's modulus was found to be 56 eV (times nanotube volume) [91]. The obtained values for Young's modulus differ significantly mainly because of the choice of the nanotube volume. Suggestions were made to chose this volume as that of a solid or hollow cylinder around the tube, or a solid hexagonal prism. It was also proposed to avoid the ambiguity due to the choice of the nanotube volume by calculating Young's modulus per unit surface of the tube or multiplied by the volume per atom of the tube. In most cases, the Young's modulus was determined numerically as the second derivative of the strain energy with respect to nanotube length.

Buckling was studied within a classical molecular-dynamics approach using Tersoff–Brenner potentials [113]. The simulations predict for a SWNTs a 30% drop in the force after buckling and that further displacement occurs at nearly constant force, i.e., linear strain energy. This picture qualitatively corresponds to the results in [110] possibly because in the latter the tubes are multi-walled and the separate walls buckle at different strains, thus broadening the discontinuity.

8.2. Bundles of SWNTs

The elastic moduli of crystalline ropes of single-walled carbon nanotubes were measured by Salvetat et al. [118]. The ropes were deposited over the pores of a membrane surface. An atomic force microscope operating in air was used to apply force midway along the suspended length of a rope and to determine directly the resulting deflection. The deflection versus force measurements showed that the nanotube response was linear and elastic for the whole range of applied forces. Rope's deflection involves both bending and shear deformations and is therefore expressed by means of the Young's and shear moduli. The estimations of these moduli yield average values $Y \approx 600$ GPa

and $G \approx 19.5$ GPa. The low value of Y compared to graphene was explained by possible interruptions or missing tubes in the ropes.

Yu et al. [119] studied the mechanical response of ropes of SWNTs under tensile load in a XYZ stage operated inside a scanning electron microscope. A piezo actuator was added onto the stage to provide the force and displacement. An AFM probe with cantilever was attached to the actuator and was used to attach the end of the rope to its sharp tip. The rope was then being stretched by application of voltage to the actuator. The tensile force was estimated from the force constant of the cantilever and its deflection. The measurements yielded Young's modulus between 320 and 1470 GPa (mean 1002 GPa). The tubes broke at strain values of 5.2% or lower and the breaking strength was found to range between 13 and 52 GPa (mean 30 GPa).

The theoretical study of the elastic moduli of ropes of SWNTs was done within force-constant models [112,120]. Young's and shear moduli were found to be weakly dependent on the number of tubes in the rope with average values of ~1 and ~0.5 TPa, respectively [112]. The elastic moduli and elastic constants of infinite ropes of identical achiral tubes with radii R from 2 to 15 Å displayed strong dependence on the tube radius [120]. In particular, the bulk modulus has a maximum of 38 TPa at $R \approx 6$ Å, which can be of importance for the application of nanotubes in reinforced composites.

9. Thermal properties

The specific heat and thermal conductivity of carbon nanotube systems are determined primarily by phonons. At low temperatures, the phonon contribution to these quantities dominates and is due primarily to acoustic phonons. The measurements yield linear specific heat and thermal conductivity above 1 K and below room temperature [121–126] while a $T^{0.62}$ behavior of the specific heat was observed below 1 K [124]. The linear temperature dependence can be explained with the linear $\boldsymbol{k}$-vector dependence of the frequency of the longitudinal and twist acoustic phonons [127]. The specific behavior of the specific heat below 1 K can be attributed to the transverse acoustic phonons with quadratic $\boldsymbol{k}$ dependence [128]. The measurements of the thermoelectric power (TEP) of nanotube systems give direct information for the type of carriers and conductivity mechanisms [129–131].

9.1. Specific heat

The measurements of the specific heat of MWNTs from 10 to 300 K [121] revealed linear dependence of the specific heat on the temperature over the entire temperature interval. This behavior was attributed to the acoustic branches of the separate layers. Mizel et al. [122] measured the specific heat of MWNTs and bundles of SWNTs with average diameter of 1.3 nm in the temperature range $1 < T < 200$ K. The MWNT data had graphite-like behavior while the bundle data had rather steep temperature dependence at low temperatures. The latter could not be described satisfactory by a model of coupled oscillators and the temperature dependence was attributed to the presence of impurities in the sample. Hone et al. [123] measured the specific heat of SWNT bundles with average tube diameter of 1.25 nm from 300 to 2 K. The experimental data was found to lie close to the theoretical curve for SWNTs above 4 K and to differ remarkably from the curves for graphene and graphite up to ~100 K. The low-temperature deviation of the measured specific heat was explained by means of a two-band Debye model, which accounts for the coupling between the nanotubes in the bundle. Recently, Lasjaunias et al. [124] measured the specific heat of SWNT

bundles down to 0.1 K. The corrected data was fitted with the combination of power laws $0.043T^{0.62} + 0.035T^3$. The presence of the sublinear term, dominant below $\sim$1 K, could not be explained.

Estimations of the electronic and phonon contributions to the low-temperature specific heat of carbon nanotubes showed that the phonon contribution is dominant down to $T = 0$ K [127]. The phonon specific heat of graphene has a quadratic temperature contribution due to longitudinal acoustic (LA) and in-plane transverse acoustic phonons, and a linear contribution due to the out-of-plane transverse acoustic (ZA) phonons. As a result, graphene has a linear specific heat below $\sim$50 K. In the case of SWNTs, force-constant calculations [83] yield linear wavevector dependence of all four acoustic branches: longitudinal, twist, and doubly-degenerate transverse ones. The resulting specific heat is linear in temperature below temperatures, corresponding to excitation of the lowest-energy optical phonons ($\sim$2.5 meV or 30 K for nanotubes (10, 10)). Based on such arguments, the observed linear specific heat of bundles could be explained. However, the recent observation of sublinear temperature dependence of the specific heat of SWNT bundles [124] could not be understood. By force-constant dynamical calculations it was demonstrated that the transverse acoustic branches have quadratic wavevector dependence near the zone center [85], which was confirmed by continuum mechanics arguments [132]. This is shown to change drastically the low-energy phonon density of states (PDOS) and the low-temperature specific heat. The PDOS is no longer constant but varies as $\omega^{-1/2}$. Furthermore, at low temperature (<1 K), only the transverse phonons are excited, giving rise to a $T^{1/2}$ dependence of the specific heat [128]. The exponent 1/2 agrees with the fitted one of 0.62 (Fig. 34).

The low-temperature specific heat of MWNTs is expected to show $T^{1/2}$ dependence up to temperatures at which the transverse branches are exhausted and the longitudinal and twist acoustic
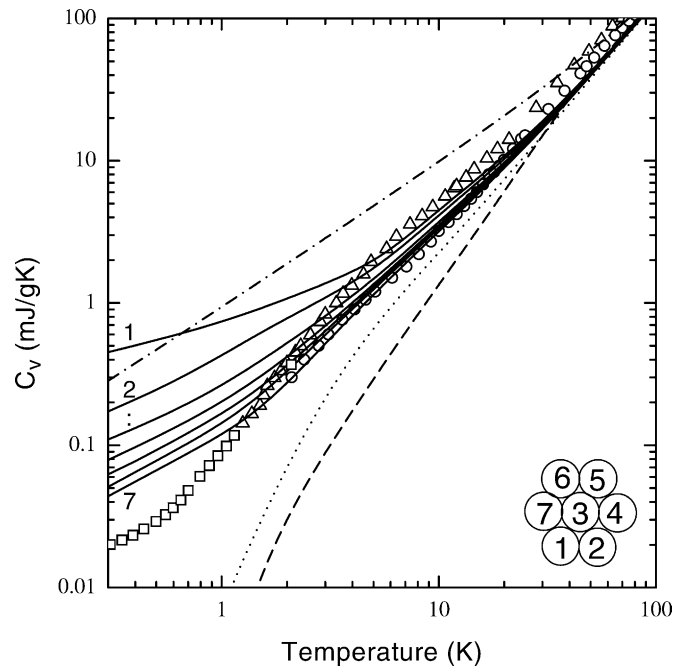

Fig. 34. Low-temperature specific heat of SWNT bundles vs. temperature. Experiment: triangles [122], circles [123], squares [124]. Calculations: graphite (dashed curve), graphene (dash–dotted curve), infinite bundles of SWNTs (dotted curves), finite bundles of 1–7 SWNTs (9, 9) (numbered solid curves) (after [128]).

branches change this dependence to a linear one in *T*. The crossover temperature decreases with the increase of the nanotube diameter. At even higher temperatures, a mixed 2D–3D behavior of the specific heat can follow due to the weak interlayer interactions in the MWNTs. In a similar way, with the increase of the size of the bundles of SWNTs, the crossover temperature from $T^{1/2}$ dependence to linear-*T* dependence decreases. At higher temperatures, the specific heat will have a mixed 2D–3D behavior due to the weak intertube interactions.

9.2. Thermal conductivity

The thermal conductivity κ of CVD-grown MWNTs measured from 4 to 300 K [121] was found to varied as T^2, similar to that of graphite, and did not show a maximum due to Umklapp scattering. The room temperature value of κ is small, which is consistent with small system size and dominance of the grain-boundary scattering.

Similar behavior was observed in the measurements of the temperature-dependent thermal conductivity of bundles of SWNTs from 8 to 350 K [125]. The thermal conductivity decreased smoothly with the decrease of T and displayed linear temperature dependence below 30 K (Fig. 35). The absence of a maximum in $\kappa(T)$ rules out phonon Umklapp scattering processes. The ratio of the thermal and electrical conductivity indicated that the thermal conductivity is dominated by phonons at all temperatures. The thermal conductivity is equal to the product of the specific heat, the phonon group velocity (squared) and the phonon relaxation time, summed over the phonon states. At low enough temperature, only the acoustic branches contribute to the specific heat. Supposing linear acoustic dependence on the wavevector, the specific heat is found linear in *T*. Then linear thermal conductivity implies constant relaxation time. The latter is true for phonon scattering off the sample boundaries. At temperatures below ~1 K, the specific heat is dominantly due to the transverse acoustic phonons, which are shown to be quadratic in the wavevector and thus yielding $T^{1/2}$ specific heat [128]. Based on similar arguments as above, it can be concluded that the very-low-*T* dependence of the thermal conductivity will vary as $T^{1/2}$.

Recently, the thermal conductivity of an individual MWNT was measured using a microfabricated suspended device [126]. The observed thermal conductivity was more than 3000 W/mK at room temperature, which is two orders of magnitude higher than the estimation of previous experiments that used macroscopic mat samples (~20 W/mK [121], ~35 W/mK [125]).). The temperature dependence of the thermal conductivity shows behavior that is absent in bulk
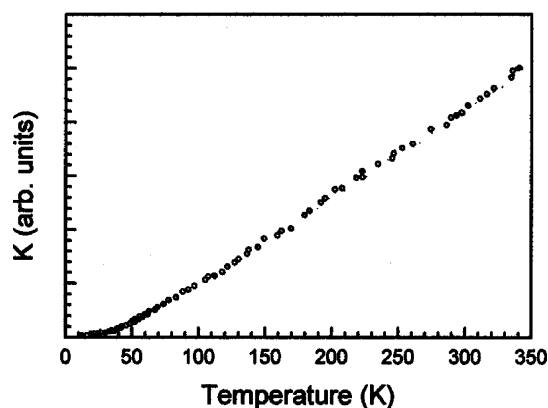

Fig. 35. Measured temperature dependence of the thermal conductivity of bundles of SWNTs (after [125]).

measurements. At low temperatures, $8 < T < 50$ K, it increases following a power law with an exponent 2.50. In the intermediate temperature range ($50 < T < 150$) it increases quadratically in T. Above this temperature range it exhibits a peak at 320 K. As the diameter of the MWNT increases, the thermal conductivity versus T becomes similar to the bulk measurements. At low temperatures, the Umklapp scattering freezes and $\kappa(T)$ follows $C(T)$. The $T^{2.5}$ dependence is due to the interlayer phonon modes giving rise to slight three-dimensional nature. The T^2 dependence is due to the higher frequency phonon modes of the separate layers. As T increases, the strong phonon-phonon Umklapp processes become more effective and the Umklapp path decreases. Once the static and Umklapp paths become equal, a peak in $\kappa(T)$ appears.

Berber et al. [133] simulated the thermal conductivity of carbon nanotubes using equilibrium and non-equilibrium molecular-dynamics. The results suggest an unusually high value of the ≈ 6600 W/mK for an isolated (10, 10) nanotube at room temperature, comparable to the thermal conductivity of graphite. These high values are associated with the large phonon mean free paths in these systems.

9.3. Thermoelectric power

The experimental study of the thermoelectric power can provide experimental confirmation of band structure calculations and throw more light on the electrical properties of SWNTs. The sign of the TEP indicates the type of the dominant current carrier. The temperature dependence of the TEP provides information about the type of conduction. The TEP of a simple metal is linear in the temperature T while that of a semiconductor has $1/T$ dependence. Therefore, the low-temperature measurements can prove whether there is an opening of an energy gap at the Fermi level.

Hone et al. [129] measured the temperature-dependent thermoelectric power of crystalline ropes of SWNTs (Fig. 36). At room temperature the TEP is positive and of moderate amplitude (~ 50 μV/K) while at low temperatures it is linear in T and approaches zero as $T \rightarrow 0$. The large positive TEP at high temperatures was attributed to hole-like carriers. The band structure calculations predict electron–hole symmetry for metallic tubes and therefore TEP should be close to zero. The non-zero TEP can be explained by breaking the electron–hole symmetry by assembling the tubes in a rope, which is accompanied with opening of an energy gap. However, the vanishing of the TEP at low
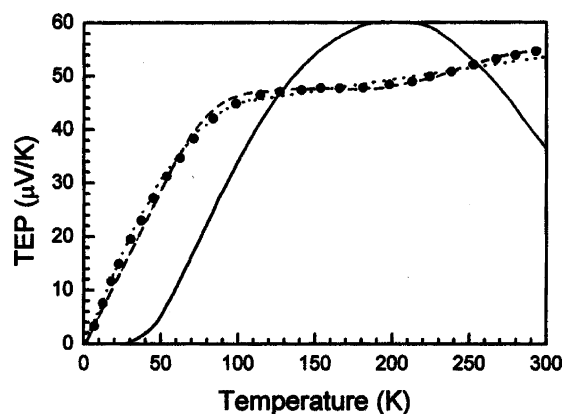

Fig. 36. Temperature dependence of the thermoelectric power of SWNT ropes: measured (filled symbols) and simulated (lines). The solid line corresponds to a model with energy gap of the metallic tubes. The discontinuous lines correspond to a model with metallic and semiconducting tubes (after [129]).

temperatures is an argument against opening of an energy gap. In order to explain the observed TEP behavior, a rope of SWNTs consisting of metallic and semiconducting tubes was considered. Modeling the TEP of the rope, it was taken into account that the TEP includes contributions from electronic effects and electron–phonon effects. The experimental data could be fitted well with the model expression for TEP only if no gap opens for the metallic tubes. The values of the fitting parameters showed that there is transfer of electrons from the metallic to the semiconducting tubes, resulting in hole-like metallic tubes and electron-like semiconducting tubes. This self-doping mechanism leads to electron–hole symmetry breaking in metallic tubes in ropes and to the observed temperature behavior of the TEP.

In measurements of the thermoelectric power of bundles of MWNTs in the range 4.2–300 K it was found that the TEP is positive over the entire temperature range [130]. The TEP has a value of $\sim$22 µV/K at 300 K and increases with the increase of temperature. A two-band model was considered in which the TEP was due to metallic band carriers and semiconducting band carriers. The TEP showed deviation from the linear temperature dependence below 30 K. In this temperature region, the resistivity had a ln T term, which indicated two-dimensional weak localization of carriers in metal. Therefore, the deviation of the TEP was attributed to changes of the transport mechanism related to localization effects of carriers in metallic tubes.

The measured thermoelectric power of SWNTs bundles prepared using M-Y catalysts (M: Fe, Co, Ni) was found positive over the entire range of temperature 10–400 K, indicating the dominant contribution of hole carriers [131]. The TEP was linear at low temperatures and had a peak in the range 80–100 K. The presence of such a peak was assigned to magnetic impurities in the bundles and was explained as a Kondo effect due to spin-dependent scattering mechanism between the magnetic moments of the impurity atoms and the spins of the conduction electrons of the nanotubes.

10. Summary

In this report, the major developments in both the basic research and the industrial application of the carbon nanotubes are reviewed. The theoretical efforts are directed to the understanding the amazing mechanical, electronic, transport, vibrational, thermal, etc., properties most of them owing their uniqueness to the quasi-one-dimensional sp^2-bonded structure of the carbon nanotubes. At laboratory level nanotubes are being applied as tips of field emission devices, elements of nanoelectronics devices, gas storage containers, reinforcement elements, etc. Nanotubes still have a wide range of unexplored potential applications in various technological areas such as aerospace, energy, automobile, medicine, or chemical industry, in which they can be used as gas adsorbents, templates, actuators, composite reinforcements, catalyst supports, probes, chemical sensors, nano-pipes, nano-reactors, ... It is now a widely-shared view that carbon-based materials are likely to be a major field in the twenty first century technology.

References

[1] H.W. Kroto, J.R. Heath, S.C. O'Brien, R.F. Curl, R.E. Smalley, C_{60}: buckminsterfullerene, Nature 318 (1985) 162.

[2] S. Iijima, Helical microtubules of graphitic carbon, Nature (London) 354 (1991) 56.

[3] S. Iijima, T. Ichihashi, Single-shell carbon nanotubes of 1-nm diameter, Nature (London) 363 (1993) 603.

[4] D.S. Bethune, C.H. Kiang, M.S. de Vries, G. Gorman, R. Savoy, J. Vazquez, R. Beyers, Cobalt-catalysed growth of carbon nanotubes with single-atomic-layer walls, Nature (London) 363 (1993) 605.

[5] M.S. Dresselhaus, G. Dresselhaus, R. Saito, Carbon fibers based on C_{60} and their symmetry, Phys. Rev. B 45 (1992) 6234.

[6] M.S. Dresselhaus, G. Dresselhaus, R. Saito, Physics of carbon nanotubes, Carbon 33 (1995) 883.

[7] M.S. Dresselhaus, G. Dresselhaus, P.C. Eklund, Science of Fullerenes and Carbon Nanotubes, Academic Press, New York, 1996.

[8] R. Saito, G. Dresselhaus, M.S. Dresselhaus, Physical Properties of Carbon Nanotubes, Imperial College Press, London, 1998.

[9] M.S. Dresselhaus, G. Dresselhaus, Ph. Avouris (Eds.), Carbon nanotubes: Synthesis, Structure, Properties, and Applications, Springer–Verlag, Berlin, 2001.

[10] G. Overney, W. Zhong, D. Tománek, Structural rigidity and low frequency vibrational modes of long carbon tubules, Z. Phys. D 27 (1993) 93–96.

[11] A.G. Rinzler, J.H. Hafner, P. Nikolaev, L. Lou, S.G. Kim, D. Tomanek, P. Nordlander, D.T. Colbert, R.E. Smalley, Unraveling nanotubes: field emission from an atomic wire, Science 269 (1995) 1550.

[12] G. Che, B.B. Lakshmi, E.R. Fisher, C.R. Martin, Carbon nanotubule menbranes for electrochemical energy storage and production, Nature 393 (1998) 346.

[13] B. Gao, A. Kelinhammes, X.P. Tang, C. Bower, Y. Wu, O. Zhou, Electrochemical intercalation of single-walled carbon nanotubes with lithium, Chem. Phys. Lett. 307 (1999) 153.

[14] A.C. Dillon, K.M. Jones, T.A. Bekkendahl, C.H. Kiang, D.S. Bethune, M.J. Heben, Storage of hydrogen in single-walled carbon nanotubes, Nature 386 (1997) 377.

[15] A. Bachtold, P. Hadley, T. Nakanishi, C. Dekker, Logic circuits with carbon nanotube transistors, Science 294 (2001) 1317.

[16] P.C. Collins, M.S. Arnold, P. Avouris, Engineering carbon nanotubes and nanotube circuits using electrical breakdown, Science 292 (2001) 706.

[17] A. Thess, R. Lee, P. Nikolaev, H. Dai, P. Petit, J. Robert, C. Xu, Y.H. Lee, S.G. Kim, A.G. Rinzler, D.T. Colbert, G.E. Scuseria, D. Tomanék, J.E. Fischer, R.E. Smalley, Crystalline ropes of metallic carbon nanotubes, Science 273 (1996) 483.

[18] M.J. Yacaman, M.M. Yoshida, L. Rendon, J.G. Santiesteban, Catalytic growth of carbon microtubules with fullerene structure, Appl. Phys. Lett. 62 (1993) 202.

[19] S. Iijima, T. Ichihashi, Y. Ando, Pentagons, Nature London 356 (1992) 776.

[20] S. Iijima, P.M. Ajayan, T. Ichihashi, Growth model for carbon nanotubes, Phys. Rev. Lett. 69 (1992) 3100.

[21] T.W. Ebbesen, P.M. Ajayan, Large-scale synthesis of carbon nanotubes, Nature (London) 358 (1992) 220.

[22] C. Journet, W.K. Maser, P. Bernier, A. Loiseau, M. Lamy de la Chapelle, S. Lefrant, P. Deniard, R. Lee, andJ.E. Fischer, Large-scale production of single-walled carbon nanotubes by the electric-arc technique, Nature (London) 388 (1997) 756.

[23] J. Liu, A.G. Rinzler, H. Dai, J.H. Hafner, R.K. Bradley, P.J. Boul, A. Lu, T. Iverson, K. Shelimov, C.B. Huffman, F. Rodriguex-Macia, D.T. Colbert, R.E. Smalley, Fullerene pipes, Science 280 (1998) 1253.

[24] R.T.K. Baker, Catalytic growth of carbon filaments, Carbon 27 (1989) 315.

[25] G.G. Tibbetts, Vapor-grown carbon fibers: status and prospectus, Carbon 27 (1989) 745.

[26] V. Ivanov, J.B. Nagy, Ph. Lambin, A. Lucas, X.B. Zhang, X.F. Zhang, D. Bernaerts, G. Van Tendeloo, S. Amelinckx, J. Van Landuyt, The study of carbon nanotubules produced by catalytic method, Chem. Phys. Lett. 223 (1994) 329.

[27] S. Amelinckx, X.B. Zhang, D. Bernaerts, Z.F. Zhang, V. Ivanov, J.B. Nagy, A formation mechanism for catalytically grown helix shaped graphite nanotubes, Science 265 (1994) 635.

[28] W.Z. Li, S.S. Xie, L.X. Qian, B.H. Chang, B.S. Zou, W.Y. Zhou, R.A. Zhao, G. Wang, Large-scale synthesis of aligned carbon Nanotubes, Science 274 (1996) 1701.

[29] S. Fana, W. Liang, H. Dang, N. Franklin, T. Tombler, M. Chapline, H. Dai, Carbon nanotube arrays on silicon substrates and their possible application, Physica E 8 (2000) 179.

[30] J. Kong, H.T. Soh, A.M. Cassell, C.F. Quate, H. Dai, Synthesis of individual single-walled carbon nanotubes on patterned silicon wafers, Nature (London) 395 (1998) 878.

[31] T. Guo, B. Nikolaev, A.G. Rinzler, D. Tomanek, D.T. Colbert, R.E. Smalley, Self-assembly of tubular fullerenes, J. Phys. Chem. 99 (1995) 10694.

[32] J.C. Charlier, A. de Vita, X. Blase, R. Car, Microscopic growth mechanisms for carbon nanotubes, Science 275 (1997) 646.

[33] J.C. Charlier, X. Blasé, A. de Vita, R. Car, Electronic structure at carbon nanotube tips, Appl. Phys. A 68 (1999) 267.

[34] Y.K. Kwon, Y.H. Lee, S.G. Kim, P. Jund, D. Tomanek, R.E. Smalley, Phys. Rev. Lett. 79 (1997) 2065.

[35] B. Nardelli, C. Brabec, A. Maiti, C. Roland, J. Bernholc, Lip–lip interactions and the growth of multi-walled carbon nanotubes, Phys. Rev. Lett. 80 (1998) 313.

[36] A. Maiti, C.J. Brabec, C.M. Roland, J. Bernholc, Theory of carbon nanotube growth, Phys. Rev. B 52 (1995) 14850.

[37] Y.H. Lee, S.G. Kim, P. Jund, D. Tomanek, Catalytic growth of single-wall carbon nanotubes: an ab initio study, Phys. Rev. Lett. 78 (1997) 2393.

[38] L.C.Qin.S. Iijima, Structure and formation of raft-like bundles of single-walled helical carbon nanotubes produced by laser evaporation, Chem. Phys. Lett. 269 (1997) 65.

[39] A. Maiti, C.J. Brabec, J. Bernholc, Kinetics of metal-catalyzed growth of single-walled carbon nanotubes, Phys. Rev. B 55 (1997) R6097.

[40] J.W. Mintmire, B.I. Dunlap, C.T. White, Are fullerene tubes metallic? Phys. Rev. Lett. 68 (1992) 631.

[41] N. Hamada, S. Sawada, A. Oshiyama, New one-dimensional conductors: graphitic microtubules, Phys. Rev. Lett. 68 (1992) 1579.

[42] R. Saito, M. Fujita, G. Dresselhaus, M.S. Dresselhaus, Electronic structure of graphene tubules based on C_{60}, Phys. Rev. B 45 (1992) 6234.

[43] Y.-K. Kwon, S. Saito, D. Tománek, Effect of intertube coupling on the electronic structure of carbon nanotube ropes, Phys. Rev. B 58 (1998) R13314.

[44] P. Delaney, H.J. Choi, J. Ihm, S.G. Louie, M.L. Cohen, Broken symmetry and pseudogaps in ropes of carbon nanotubes, Phys. Rev. B 60 (1999) 7899.

[45] X. Blase, L.X. Benedict, E.L. Shirley, S.G. Louie, Phys. Rev. Lett. 72 (1994) 1878.

[46] H. Ajiki, T. Ando, Aharonov–Bohm effect in carbon nanotubes, Physica B 201 (1994) 349.

[47] J.W. Mintmire, C.T. White, Universal density of states for carbon nanotubes, Phys. Rev. Lett. 81 (1998) 2506.

[48] H. Kataura, Y. Kumazawa, Y. Maniwa, I. Umezu, S. Suzuki, Y. Ohtsuka, Y. Achiba, Optical properties of single-wall carbon nanotubes, Synth. Metals 103 (1999) 2555.

[49] Y.-K. Kwon, D. Tománek, Electronic and structural properties of multiwall carbon nanotubes, Phys. Rev. B 58 (1998) R16001.

[50] S. Reich, C. Thomsen, P. Ordejón, Electronic band structure of isolated and bundled carbon nanotubes, Phys. Rev. B 65 (2002) 155411.

[51] S. Kazaoui, N. Minami, R. Jacquemin, H. Kataura, Y. Achiba, Amphoteric doping of single-wall carbon-nanotube thin films as probed by optical absorption spectroscopy, Phys. Rev. B 60 (1999) 13339.

[52] J. Hwang, H.H. Gommans, A. Ugawa, H. Tashiro, R. Haggenmueller, K.I. Winey, J.E. Fischer, D.B. Tanner, A.G. Rinzler, Polarized spectroscopy of aligned single-wall carbon nanotubes, Phys. Rev. B 62 (2000) R13310.

[53] Z.M. Li, Z.K. Tang, H.J. Liu, N. Wang, C.T. Chan, R. Saito, S. Okada, G.D. Li, J.S. Chen, N. Nagasawa, S. Tsuda, Polarized absorption spectra of single-walled 4 Å carbon nanotubes aligned in channels of an AlPO4-5 single crystal, Phys. Rev. Lett. 87 (2001) 127401.

[54] L.X. Benedict, S.G. Louie, M.L. Cohen, Static polarizability of single-wall carbon nanotubes, Phys. Rev. B 52 (1995) 8541.

[55] X. Liu, T. Pichler, M. Knupfer, M.S. Golden, J. Fink, H. Kataura, Y. Achiba, Detailed analysis of the mean diameter and diameter distribution of single-wall carbon nanotuibes from their optical response, Phys. Rev. B 66 (2002) 45411.

[56] T. Pichler, M. Knupfer, M.S. Golden, J. Fink, A. Rinzler, R.E. Smalley, Localized and delocalized electronic states in single-wall carbon nanotubes, Phys. Rev. Lett. 80 (1998) 4729.

[57] M. Kociak, L. Henrard, O. Stéphan, K. Suenaga, C. Colliex, Plasmons in layered nanospheres and nanotubes investigated by spatially resolved electron energy-loss spectroscopy, Phys. Rev. B 61 (2000) 13963.

[58] L. Langer, V. Bayot, E. Grivei, J.P. Issi, J.P. Heremans, C.H. Olk, L. Stockman, C. Van Haesendonck, Y. Bruynseraede, Quantum transport in a multi-walled carbon nanotube, Phys. Rev. Lett. 76 (1996) 479.

[59] T.W. Ebbesen, H.J. Lezec, H. Hiura, J.W. Bennett, H.F. Ghaemi, T. Thio, Nature (London) 382 (1996) 54.

[60] H. Dai, E.W. Wong, C.M. Lieber, Science 272 (1996) 523.

[61] M. Bockrath, D.H. Cobden, P.L. McEuen, N.G. Chopra, A. Zettle, A. Thess, R.E. Smalley, Single-electron transport in ropes of carbon nanotubes, Science 275 (1997) 1922.

[62] J.E. Fischer, H. Dai, A. Thess, R. Lee, N.M. Hanjani, D.L. Dehaas, R.E. Smalley, Metallic resistivity in crystalline ropes of single-wall carbon nanotubes, Phys. Rev. B 55 (1997) R4921.

[63] S.J. Tans, M.H. Devoret, H. Dai, A. Thess, R. Smalley, L.J. Geerlings, C. Dekker, Individual single-wall carbon nanotubes as quantum wires, Nature (London) 386 (1997) 474.

[64] J. Voit, One-dimensional Fermi liquid, Rep. Prog. Phys. 58 (1995) 977.

[65] C. Kane, L. Balents, M.P.A. Fisher, Coulomb interactions and mesoscopic effects in carbon nanotubes, Phys. Rev. Lett. 97 (1997) 5086.

[66] M. Bockrath, D.H. Cobden, J. Lu, A.G. Ronzler, R.E. Smalley, L. Balents, P.L. McEuen, Luttinger-liquid behaviour in carbon nanotubes, Nature (London) 397 (1999) 598.

[67] Z. Yao, C.L. Kane, C. Dekker, High-field electrical transport in single-wall carbon nanotubes, Phys. Rev. Lett. 84 (2000) 2941.

[68] S.J. Tans, A.R.M. Verschueren, C. Dekker, Room-temperature transistor based on a single carbon nanotube, Nature (London) 393 (1998) 49.

[69] R. Martel, T. Schmidt, H.R. Shea, T. Hertel, Ph. Avouris, Single- and multi-wall carbon nanotube field-effect transistors, Appl. Phys. Lett. 73 (1998) 2447.

[70] H.W.C. Postma, T. Teepen, Z. Yao, M. Grifoni, C. Dekker, Carbon nanotube single-electron transistors at room temperature, Science 293 (2001) 76.

[71] (a) B.I. Dunlap, Connecting carbon tubules, Phys. Rev. B 46 (1992) 1933;
     (b) B.I. Dunlap, Relating carbon tubules, Phys. Rev. B 49 (1994) 5643;
     (c) B.I. Dunlap, Constraints on small graphitic helices, Phys. Rev. B 50 (1994) 8134.

[72] R. Saito, G. Dresselhaus, M.S. Dresselhaus, Tunneling conductance of connected carbon nanotubes, Phys. Rev. B 53 (1996) 2044.

[73] L. Chico, V.H. Crespi, L.X. Benedict, S.G. Louie, M.L. Cohen, Pure carbon nanoscale devices: heterojunctions, Phys. Rev. Lett. 76 (1996) 971.

[74] J.C. Charlier, T.W. Ebbesen, Ph. Lambin, Structural and electronic properties of pentagon–heptagon pair defects in carbon nanotubes, Phys. Rev. B 53 (1996) 11108.

[75] A. Fonseca, E.A. Perpète, P. Galet, B. Champagne, J.B. Nagy, J.M. André, Ph. Lambin, A.A. Lucas, Quantum chemical evaluation of the knee angle in the (5, 5)–(9, 0) coiled carbon nanotube, J. Phys. B 29 (1996) 4915.

[76] C. Zhou, J. Kong, E. Yenilmez, H. Dai, Dodulated chemical doping of individual carbon nanotubes, Science 290 (2000) 1552.

[77] C. Papapdopoulos, A. Rakitin, J. Li, A.S. Vedeneev, J.M. Xu, Electronic transport in Y-junction carbon nanotubes, Phys. Rev. Lett. 85 (2000) 3476.

[78] M.S. Fuhrer, J. Nygård, L. Shih, Y.G. Yoon, M.S.C. Mazzoni, H.J. Choi, J. Ihm, S.G. Louie, A. Zettl, P.L. McEuen, Crossed nanotube junctions, Science 288 (2000) 494.

[79] P.G. Collins, A. Zettl, H. Bando, A. Thess, R.E. Smalley, Nanotube nanodevices, Science 278 (1997) 100.

[80] Z. Yao, H.W.C. Postma, L. Balents, C. Dekker, Carbon nanotube intramolecular junctions, Nature (London) 402 (1999) 273.

[81] J. Li, C. Papadopoulos, J.M. Xu, Growing Y-junction carbon nanotubes, Nature (London) 402 (1999) 253.

[82] P.C. Eklund, J.M. Holden, R.A. Jishi, Vibrational modes of carbon nanotubes spectroscopy and theory, Carbon 33 (1995) 959.

[83] R. Saito, T. Takeya, T. Kimura, G. Dresselhaus, M.S. Dresselhaus, Raman intensity of single-wall carbon nanotubes, Phys. Rev. B 57 (1998) 4145.

[84] A. Charlier, E. McRae, M.F. Charlier, A. Spire, S. Foster, Lattice dynamics study of zigzag and armchair carbon nanotubes, Phys. Rev. B 57 (1998) 6689.

[85] V.N. Popov, V.E. Van Doren, M. Balkanski, Lattice dynamics of single-walled carbon nanotubes, Phys. Rev. B 59 (1999) 8355.

[86] J. Yu, R.K. Kalia, P. Vashishta, Phonons in graphitic tubules: a tight-binding molecular dynamics study, J. Chem. Phys. 103 (1995) 6697.

[87] M. Menon, E. Richter, K.R. Subbaswamy, Structural and vibrational properties of fullerenes and nanotubes in a nonorthogonal tight-binding scheme, J. Chem. Phys. 104 (1996) 5875.

[88] A.M. Rao, E. Richter, S. Bandow, B. Chase, P.C. Eklund, K.W. Williams, M. Menon, K.R. Subbaswamy, A. Thess, R.E. Smalley, G. Dresselhaus, M.S. Dresselhaus, Diameter-selective Raman scattering from vibrational modes in carbon nanotubes, Science 275 (1997) 187.

[89] D. Kahn, P. Lu, Vibrational modes of carbon nanotubes and nanoropes, Phys. Rev. B 60 (1999) 6535.

[90] J. Kürti, G. Kresse, H. Kuzmany, First-principles calculations of the radial breathing mode of single-wall carbon nanotubes, Phys. Rev. B 58 (1998) 8869.

[91] D. Sánchez-Portal, E. Artacho, J.M. Soler, A. Rubio, andP. Ordejón, Ab initio structural, elastic, and vibrational properties of carbon nanotubes, Phys. Rev. B 59 (1999) 12678.

[92] O. Dubay, G. Kresse, Accurate density functional calculations for the phonon dispersion relations of graphite layer and carbon nanotubes, Phys. Rev. B 67 (2003) 035401.

[93] A.M. Rao, A. Jorio, M.A. Pimenta, M.S.S. Dantas, R. Saito, G. Dresselhaus, M.S. Dresselhaus, Polarized Raman study of aligned multi-walled carbon nanotubes, Phys. Rev. Lett. 84 (2000) 1820.

[94] A. Jorio, G. Dresselhaus, M.S. Dresselhaus, M. Souza, M.S.S. Dantas, M.A. Pimenta, A.M. Rao, R. Saito, C. Liu, H.M. Cheng, Polarized Raman study of single-wall semiconducting carbon nanotubes, Phys. Rev. Lett. 85 (2000) 2617.

[95] J. Azoulay, A. Débarre, A. Richard, P. Tchénio, S. Bandow, S. Iijima, Polarised Raman spectroscopy on a single class of single-wall nanotubes by nano surface-enhanced scattering, Chem. Phys. Lett. 331 (2000) 347.

[96] G.S. Duesberg, I. Loa, M. Burghard, K. Syassen, S. Roth, Polarized Raman spectroscopy on isolated single-wall carbon nanotubes, Phys. Rev. Lett. 85 (2000) 5436.

[97] A. Jorio, M.A. Pimenta, A.G. Souza Filho, G.G. Samsonidze, A.K. Swan, M.S. Ünlü, B.B. Goldberg, R. Saito, G. Dresselhaus, M.S. Dresselhaus, Resonance Raman spectra of carbon nanotubes by cross-polarized light, Phys. Rev. Lett. 90 (2003) 107403.

[98] R.A. Jishi, M.S. Dresselhaus, G. Dresselhaus, Symmetry properties of chiral carbon nanotubules, Phys. Rev. B 47 (1993) 16671.

[99] R.A. Jishi, L. Venkataraman, M.S. Dresselhaus, G. Dresselhaus, Phonon modes in carbon nanotubules, Chem. Phys. Lett. 209 (1993) 77.

[100] W.S. Bacsa, D. Ugarte, A. Châtelain, W.A. de Heer, High-resolution electron microscopy and inelastic light scattering of purified multishelled carbon nanotubes, Phys. Rev. B 50 (1994) 15473.

[101] V.N. Popov, V.E. Van Doren, M. Balkanski, Elastic properties of single-walled carbon nanotubes, Phys. Rev. B 61 (2000) 3078.

[102] A. Jorio, R. Saito, J.H. Hafner, C.M. Lieber, M. Hunter, T. McClure, G. Dresselhaus, M.S. Dresselhaus, Structural (n, m)determination of isolated single-wall carbon nanotubes by resonant Raman scattering, Phys. Rev. Lett. 86 (2001) 1118.

[103] R.R. Bacsa, A. Peigny, Ch. Laurent, P. Peuch, W.S. Bacsa, Chirality of internal metallic and semiconducting carbon nanotubes, Phys. Rev. B 65 (2002) 161404.

[104] X. Zhao, Y. Ando, L.C. Qin, H. Kataura, Y. Maniwa, R. Saito, Multiple splitting of G-band modes from individual multi-walled carbon nanotubes, Appl. Phys. Lett. 81 (2002) 2550.

[105] A. Jorio, A.G. Souza Filho, V.W. Brar, A.K. Swan, M.S. Ünlü, B.B. Goldberg, A. Righi, J.H. Hafner, C.M. Lieber, R. Saito, G. Dresselhaus, M.S. Dresselhaus, Polarized resonant Raman study of isolated single-wall carbon nanotubes: symmetry selection rules, Phys. Rev. B 65 (2002) 121402.

[106] J. Maultzsch, S. Reich, C. Thomsen, Raman scattering in carbon nanotubes revisited, Phys. Rev. B 65 (2002) 2333402.

[107] D.H. Robertson, D.W. Brenner, J.W. Mintmire, Energetics of nanoscale graphitic tubules, Phys. Rev. B 45 (1992) 12592.

[108] M.M.J. Treacy, T.W. Ebbesen, andJ.M. Gilson, Exceptionally high Young's modulus observed for individual carbon nanotubes, Nature (London) 381 (1996) 678.

[109] A. Krishnan, E. Dujardin, T.W. Ebbesen, P.N. Yianilos, M.M.J. Treacy, Young's modulus of single-walled nanotubes, Phys. Rev. B 58 (1998) 14013.

[110] E.W. Wong, P.E. Sheehan, C.M. Lieber, Nanobeam mechanics: elasticity, strength and toughness of nanorods and nanotubes, Science 277 (1997) 1971.

[111] M.F. Yu, O. Lourie, M.J. Dyer, K. Moloni, T.F. Kelly, R.S. Ruoff, Strength and breaking mechanism of multi-walled carbon nanotubes under tensile load, Science 287 (2000) 637.

[112] J.P. Lu, Elastic properties of carbon nanotubes and nanoropes, Phys. Rev. Lett. 79 (1997) 1297.

[113] B.I. Yakobson, C.J. Brabec, J. Bernholc, Nanomechanics of carbon tubes: instabilities beyond linear response, Phys. Rev. Lett. 76 (1996) 2511.

[114] C.F. Cornwall, L.T. Wille, Elastic properties of single-walled carbon nanotubes in compression, Solid State Commun. 101 (1997) 555.

[115] E. Hernández, C. Goze, P. Bernier, A. Rubio, Elastic properties of C and $B_xC_yN_z$ composite nanotubes, Phys. Rev. Lett. 80 (1998) 4502.

[116] R.L. Jacobsen, T.M. Tritt, J.R. Guth, A.C. Ehrlich, D.J. Gillespie, Mechanical properties of vapor-grown carbon fiber, Carbon 33 (1995) 1217.

[117] J.-P. Salvetat-Delmotte, A. Rubio, Mechanical properties of carbon nanotubes: a fiber digest for beginners, Carbon 40 (2002) 1729.

[118] J.P. Salvetat, G.A.D. Briggs, J.M. Bonard, R.R. Bacsa, A.J. Kulik, T. Stöckli, N.A. Burnham, L. Forró, Elastic and shear moduli of single-walled carbon nanotube ropes, Phys. Rev. Lett. 82 (1999) 944.

[119] M.F. Yu, B.F. Files, S. Arepalli, R.S. Ruoff, Tensile loading of ropes of single wall carbon nanotubes and their mechanical properties, Phys. Rev. Lett. 84 (2000) 5552.

[120] V.N. Popov, V.E. Van Doren, M. Balkanski, Elastic properties of crystals of single-walled carbon nanotubes, Solid State Commun. 114 (2000) 395.

[121] W. Yi, L. Lu, D.L. Zhang, Z.W. Pan, S.S. Xie, Linear specific heat of carbon nanotubes, Phys. Rev. B 59 (1999) R9015.

[122] A. Mizel, L.X. Benedict, M.L. Cohen, S.G. Louie, A. Zettl, N.K. Budraa, W.P. Beyermann, Analysis of the low-temperature specific heat of multi-walled carbon nanotubes and carbon nanotube ropes, Phys. Rev. B 60 (1999) 3264.

[123] J. Hone, B. Batlogg, Z. Benes, A.T. Johnson, J.E. Fischer, Quantized Phonon Spectrum of Single-Wall Carbon Nanotubes, Science 289 (2000) 1730.

[124] J.C. Lasjaunias, K. Biljakoviæ, Z. Benes, J.E. Fischer, P. Monceau, Low-temperature specific heat of single-wall carbon nanotubes, Phys. Rev. B 65 (2002) 113409.

[125] J. Hone, M. Whitney, C. Piskoti, A. Zettl, Thermal conductivity of single-walled carbon nanotubes, Phys. Rev. B 59 (1999) R2514.

[126] P. Kim, L. Shi, A. Majumdar, P.L. McEuen, Thermal transport measurements of individual multi-walled nanotubes, Phys. Rev. Lett. 87 (2001) 215502.

[127] L. X Benedict, S. G Louie, M.L. Cohen, Heat capacity of carbon nanotubes, Solid State Comm. 100 (1996) 177.

[128] V.N. Popov, Low-temperature specific heat of nanotube systems, Phys. Rev. B 66 (2002) 153408.

[129] J. Hone, I. Ellwood, M. Muno, A. Mizal, M.L. Cohen, A. Zettl, A.G. Rinzler, R.E. Smalley, Thermoelectric power of single-walled carbon nanotubes, Phys. Rev. Lett. 80 (1998) 1042.

[130] M. Tian, F. Li, L. Chen, Z. Mao, Thermoelectric power behavior in carbon nanotubule bundles from 4.2 to 300 K, Phys. Rev. B 58 (1998) 1166.

[131] L. Grigorian, G.U. Sumanasekera, A.L. Loper, S.L. Fang, J.L. Allen, P.C. Eklund, Giant thermopower in carbon nanotubes: a one-dimensional Kondo system, Phys. Rev. B 60 (1999) R11309.

[132] G.D. Mahan, Oscillations of a thin hollow cylinder: carbon nanotubes, Phys. Rev. B 63 (2002) 235402.

[133] S. Berber, Y.K. Kwon, D. Tománek, Unusually high thermal conductivity of carbon nanotubes, Phys. Rev. Lett. 84 (2000) 4613.